
AFRL-AFOSR-VA-TR-2019-0056

# Tunable Multifunctional Organic Thermal and Thermoelectric Materials

**Shannon Yee**
**GEORGIA TECH RESEARCH CORPORATION**

**01/04/2019**
**Final Report**



Air Force Research Laboratory
AF Office Of Scientific Research (AFOSR)/ RTB2
Arlington, Virginia 22203
Air Force Materiel Command

# REPORT DOCUMENTATION PAGE

*Form Approved*
*OMB No. 0704-0188*



| **1. REPORT DATE** *(DD-MM-YYYY)* | **2. REPORT TYPE** | **3. DATES COVERED** *(From - To)* |
|---|---|---|
| 01/03/2019 | Final Report | 15 April 2015 to 14 October 2018 |

**4. TITLE AND SUBTITLE**
Tunable Multifunctional Organic Thermal and Thermoelectric Materials

**5a. CONTRACT NUMBER**
FA9550-15-1-0145

**5b. GRANT NUMBER**

**5c. PROGRAM ELEMENT NUMBER**

**6. AUTHOR(S)**
Shannon Yee

**5d. PROJECT NUMBER**

**5e. TASK NUMBER**

**5f. WORK UNIT NUMBER**

**7. PERFORMING ORGANIZATION NAME(S) AND ADDRESS(ES)**
GEORGIA TECH RESEARCH CORPORATION
505 10TH ST NW
ATLANTA GA 30318-5775

**8. PERFORMING ORGANIZATION REPORT NUMBER**

**9. SPONSORING/MONITORING AGENCY NAME(S) AND ADDRESS(ES)**
AF OFFICE OF SCIENTIFIC RESEARCH
875 NORTH RANDOLPH STREET, RM 3112
ARLINGTON VA 22203-1954

**10. SPONSOR/MONITOR'S ACRONYM(S)**

**11. SPONSOR/MONITOR'S REPORT NUMBER(S)**

**12. DISTRIBUTION/AVAILABILITY STATEMENT**
Distribution A - Approved for Public Release

**13. SUPPLEMENTARY NOTES**
None

**14. ABSTRACT**
This is the final report for AFOSR-YIP that aimed to develop the fundamental knowledge to control thermal and thermoelectric transport in organic and organic-inorganic hybrid/composite materials.

**15. SUBJECT TERMS**
organic thermoelectrics, organic thermal transport, metal coordinated polymers

| **16. SECURITY CLASSIFICATION OF:** | | | **17. LIMITATION OF ABSTRACT** | **18. NUMBER OF PAGES** | **19a. NAME OF RESPONSIBLE PERSON** |
|---|---|---|---|---|---|
| **a. REPORT** | **b. ABSTRACT** | **c. THIS PAGE** | | 40 | **19b. TELEPHONE NUMBER** *(Include area code)* |

## INSTRUCTIONS FOR COMPLETING SF 298

**1. REPORT DATE.** Full publication date, including day, month, if available. Must cite at least the year and be Year 2000 compliant, e.g. 30-06-1998; xx-06-1998; xx-xx-1998.

**2. REPORT TYPE.** State the type of report, such as final, technical, interim, memorandum, master's thesis, progress, quarterly, research, special, group study, etc.

**3. DATE COVERED.** Indicate the time during which the work was performed and the report was written, e.g., Jun 1997 - Jun 1998; 1-10 Jun 1996; May - Nov 1998; Nov 1998.

**4. TITLE.** Enter title and subtitle with volume number and part number, if applicable. On classified documents, enter the title classification in parentheses.

**5a. CONTRACT NUMBER.** Enter all contract numbers as they appear in the report, e.g. F33315-86-C-5169.

**5b. GRANT NUMBER.** Enter all grant numbers as they appear in the report. e.g. AFOSR-82-1234.

**5c. PROGRAM ELEMENT NUMBER.** Enter all program element numbers as they appear in the report, e.g. 61101A.

**5e. TASK NUMBER.** Enter all task numbers as they appear in the report, e.g. 05; RF0330201; T4112.

**5f. WORK UNIT NUMBER.** Enter all work unit numbers as they appear in the report, e.g. 001; AFAPL30480105.

**6. AUTHOR(S).** Enter name(s) of person(s) responsible for writing the report, performing the research, or credited with the content of the report. The form of entry is the last name, first name, middle initial, and additional qualifiers separated by commas, e.g. Smith, Richard, J, Jr.

**7. PERFORMING ORGANIZATION NAME(S) AND ADDRESS(ES).** Self-explanatory.

**8. PERFORMING ORGANIZATION REPORT NUMBER.** Enter all unique alphanumeric report numbers assigned by the performing organization, e.g. BRL-1234; AFWL-TR-85-4017-Vol-21-PT-2.

**9. SPONSORING/MONITORING AGENCY NAME(S) AND ADDRESS(ES).** Enter the name and address of the organization(s) financially responsible for and monitoring the work.

**10. SPONSOR/MONITOR'S ACRONYM(S).** Enter, if available, e.g. BRL, ARDEC, NADC.

**11. SPONSOR/MONITOR'S REPORT NUMBER(S).** Enter report number as assigned by the sponsoring/ monitoring agency, if available, e.g. BRL-TR-829; -215.

**12. DISTRIBUTION/AVAILABILITY STATEMENT.** Use agency-mandated availability statements to indicate the public availability or distribution limitations of the report. If additional limitations/ restrictions or special markings are indicated, follow agency authorization procedures, e.g. RD/FRD, PROPIN, ITAR, etc. Include copyright information.

**13. SUPPLEMENTARY NOTES.** Enter information not included elsewhere such as: prepared in cooperation with; translation of; report supersedes; old edition number, etc.

**14. ABSTRACT.** A brief (approximately 200 words) factual summary of the most significant information.

**15. SUBJECT TERMS.** Key words or phrases identifying major concepts in the report.

**16. SECURITY CLASSIFICATION.** Enter security classification in accordance with security classification regulations, e.g. U, C, S, etc. If this form contains classified information, stamp classification level on the top and bottom of this page.

**17. LIMITATION OF ABSTRACT.** This block must be completed to assign a distribution limitation to the abstract. Enter UU (Unclassified Unlimited) or SAR (Same as Report). An entry in this block is necessary if the abstract is to be limited.

FA9550-15-1-0145

2015-
2018

# Tunable Multifunctional Organic Thermal and Thermoelectric Materials

SHANNON YEE

**Project Narrative Overview:**

***The primary objective of this AFOSR-YIP was to develop the fundamental understanding to control the thermal and thermoelectric (TE) transport properties in organic and organic-inorganic hybrid/composite materials and interfaces.*** These materials have broad application in defense technologies including: remote power generation, flexible electronic cooling, personal cooling, thermal shielding, TE sensors/displays/chromics, structural insulation, battery cooling, and thermal cloaking. In many of these applications, the active materials are multifunctional, and, therefore, control and tunablility of thermal properties across many material domains and over many orders of magnitude is necessary.

In this AFOSR-YIP, I intended to develop the core expertise in controlling thermal and TE transport properties in polymers and other amorphous organic materials. ***Polymers and other amorphous organic materials are especially interesting because, unlike many inorganic materials, electron-phonon coupling in these materials heavily influences the thermal and thermoelectric transport***. The discrete vibrational modes (similar to phonons) in polymer and amorphous materials behave differently than crystalline inorganic materials. Even with the lack of order, coherent thermal vibrations, commonly referred to as vibrons consisting of propagons, diffusons and locon,[3] dominate the thermal and TE transport. The specific tasks of this project are divided into two thrusts: ***thermoelectric transport*** and ***thermal transport.*** The first thrust centers on the Strategic Design of High Performance Organic Thermoelectric (OTE) Materials. The second thrust centers on developing Multifunctional Lightweight Organic Thermal Materials (OTMs).

1. Improve the performance of pre-existing best-in-class OTE materials by strategically and rationally modifying their chemistry, structure, and processing conditions.

2. Demonstrate how electron-phonon coupling in organic and organic-inorganic hybrid/composite materials breaks fundamental correlations in thermoelectric transport properties and leads to new transport paradigms.

3. Develop new device architectures and capabilities of OTE materials by leveraging their unique processing and manufacturing strengths.

4. Investigate multifunctional low thermal conductivity and low-density nanoporous polymers and polymer composite materials.

5. Investigate multifunctional high thermal conductivity, low-density polymer composite and nanofoam materials.

6. Study the effects of processing on structure to control the thermal conductivity across many orders of magnitude in multifunctional materials

**Summary of AFOSR-YIP Results**

Overall this AFOSR-YIP resulted in 12 publication, and helped support 2 graduate students (Akanksha Menon and Rylan Wolfe) achieve their PhDs. Dr. Akanksha Menon is currently a postdoc at Lawrence Berkeley National Laboratory and Dr. Rylan Wolfe is currently working for Eli Lilly and Company in their Chemistry division. This AFOSR-YIP also partially supported Mr. Sampath Kommandur, who is scheduled to graduate with his PhD this spring, and Dr. David Rodin who recently graduated and will be working for Siemens.

**Summary of First Year Accomplishment (1st Year)**

In the first year, efforts contributing to several focus area objectives were made. During this year: (1) best in-class OTE materials were synthesized, (3) new OTE device architecture developments, (4) low thermal conductivity measurements systems were created, and (6) processing and structural control of thermal materials were explored. One publication resulted from the first-year effort.

1. A. Menon*, S. Yee, "Design of a polymer thermoelectric generator using radial architecture," *Journal of Applied Physics*, **119**, 055501, 2016.

**Summary of Second Year Accomplishments (2nd Year)**

In the second year, efforts expanded on several of the focus area objectives and new objectives were undertaken. During this year, (1) we continued to improve best-in class OTE materials through modified synthesis, (2) we observed thermopower and conductivity breaking thermoelectric correlations adding evidence that the hypothesis that electron-phonon coupling may lead to new transport paradigms, (3) new architectures for electrical interconnects of OTE devices have been explored, and (6) an anisotropic thermal conductivity technique has been developed to study thermal transport across many orders of magnitude. Four publications have resulted from this second-year effort.

1. A. Menon*, O. Meek, A. Eng, S. Yee, "Radial Thermoelectric Generator Fabricated from N- and P-type Conducting Polymers" *Journal of Applied Polymer Science*, **134,** 3, 2016.

2. A. Menon*, E. Unzular, R. Wolfe, J. Reynolds, S. Marder, S. Yee, "Metallo-organic n-type thermoelectrics: Emphasizing advances in nickel-ethenetetrathiolates" *Journal of Applied Polymer Science*, **134**, 3, 2016.

3. D. Rodin*, S. Yee "Simultaneous measurement of in-plane and through-plane thermal conductivity using beam-offset frequency domain thermoreflectance" *Review of Scientific Instruments,* **88**, 014902, 2016

4. S. Kommandur*, S. Yee "An Empirical Model to Predict Temperature Dependent Thermal Conductivity of Amorphous Polymers" *Journal of Polymer Science,* **55**, 15,1160-1170

***As a special note***, our contributions to the *Journal of Applied Polymer Science* were part of a special issue on Polymer Thermoelectrics, for which we were awarded the cover art.

**Summary of Third Year Accomplishments (3rd Year)**

In the third year, efforts were focused on "going deeper" with the existing class OTE materials. During this year, (1) we maximized the thermoelectric properties of Ni-ETT and achieved the highest performing solution processible n-type thermoelectric materials, (2) showed how OTE properties are correlated, (3) developed interconnect patterns that enable printed thermoelectric devices, (4) explored anisotropic thermal conductivity and reported the first measure of in-plane and through-plane thermal conductivity in N2200 and P3HT thin-films, which helped us to understand (6) how processing can be used to control thermal conductivity. Overall, five publications have resulted from this third-year effort.

1. K. Gordiz*, A. Menon*, S. Yee, "Interconnect patterns for printed organic thermoelectric devices with large fill factors," *Journal of Applied Physics,* **122**, 124507, 2017

2. S. Kommandur*, S. Yee, "A suspended 3-omega technique to measure the anisotropic thermal conductivity of semiconducting polymers", *Review of Scientific Instruments,* 114905, 2018

3. A. Menon*, R. Wolfe, S. Marder, J. Reynolds, S. Yee, "Systematic Power Factor Enhancement in n-type NiETT/PVDF Composite Films," *Advanced Functional Materials*, 1801620, 2018

4. R. Wolfe*, A. Menon*, T. Fletcher, S. Marder, J. Reynolds, S. Yee "Simultaneous Enhancement in Thermoelectric Properties of n-type NiETT/PVDF Composite Films by Annealing," *Advanced Functional Materials*, 1803275, 2018

5. S. Gregory*, A. Menon*, Shuyang Ye, D. Seferos, J. Reynolds, S. Yee "Effect of Heteroatom and Doping on the Thermoelectric Properties of Poly(Chalcogenophenes)," *Advanced Energy Materials*, 1802419, 2018

**Summary of No-Cost-Extension Period Accomplishments (3rd+ Year)**

During the no-cost-extension period (April 2018-August 2018), additional manuscripts were written for publication. Of note, we were invited to write a Progress Report for a special issue of Advanced Electronic Materials focusing on our progress advancing the field of n-type metal coordinated polymer thermoelectrics.

1. A. Menon*, R. Wolfe, S. Kommandur, S. Yee, "Progress in Nickel-Coordinated Polymers as Intrinsically Conducting n-type Thermoelectric Materials," *Advanced Electronic Materials,* (accepted) – Invited Progress Report

2. R. Wolfe*, A. Menon, S. Marder, J. Reynolds, S. Yee, "Thermoelectric Performance of n-type Poly(Ni-tetrathiooxalate) as a Counterpart to Poly(Ni-ethenetetrathiolate): NiTTO vs. NiETT," *Advanced Electronic Materials*, (under review)

**New Understanding and Model of Thermal Transport in Polymers**

During this AFOSR-YIP, we were able to enable the capabilities to measure and model the thermal conductivity of polymers at low temperatures. Thermal conductivity in crystalline materials has been theoretically and experimentally studied in good detail, but there is a need for more accurate models for amorphous and polymeric materials. Polymeric thermal conductivity exhibits a plateau-like transition at temperatures around 10 K, which is not well accounted for by existing crystalline models. During this AFOSR-YIP we created an empirical model that can predict temperature dependent thermal conductivity of amorphous polymers. The model is based on kinetic theory and accounts for three sets of vibrational modes in polymers (propagons, diffusons, and locons), and is developed using classical expressions, results of previous simulations, and our own experimental data gathered at low temperatures (~10 K). Fundamental material properties like density, monomer molecular weight, and speed of sound are the only input parameters. The model provides estimates for the locations of transitions between different sets of vibrational modes, an upper limit for the thermal conductivity, and temperature dependent thermal conductivity, which are in good agreement with experimental data

Atomic vibrations are responsible for thermal conduction in solids and are a primary contributing mechanism to thermal conductivity. In metals and other crystalline materials, the electrons and the lattice vibrations (*i.e.,* phonons) contribute to the thermal transport. The

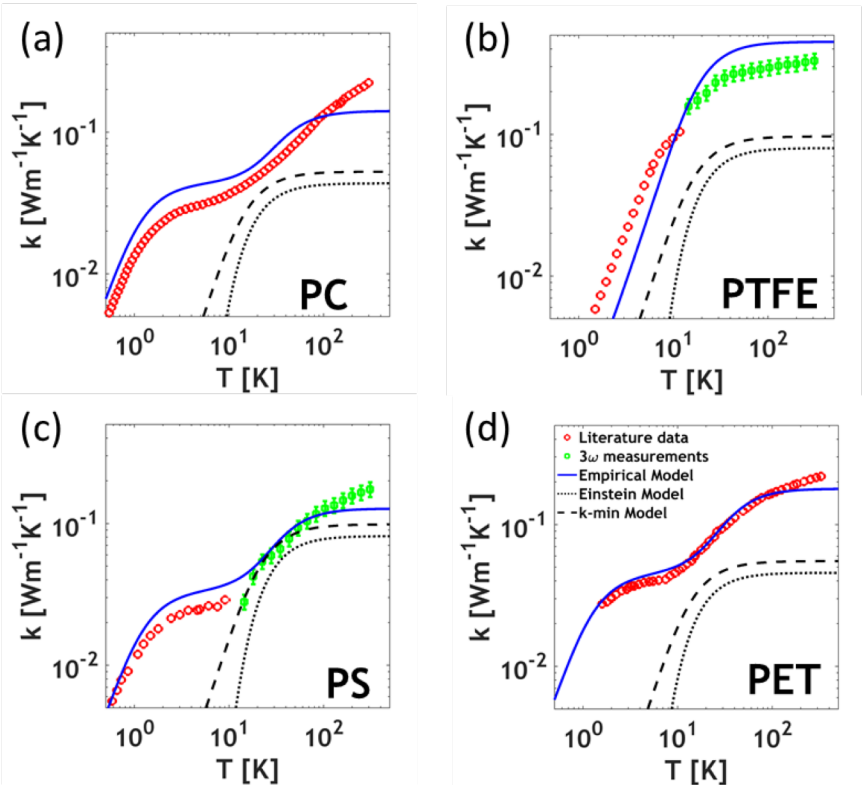


Figure 1. Literature values of experimental thermal conductivity (red hollow circles), our measurements with 3-omega technique (green squares with error bars) and the predictions based on our empirical model (solid blue line) for four different polymers. Figures (a) through (d) are for PET, PTFE, PS, and PC, respectively. Also shown are the predictions of the Einstein model (···) and k-min model (---). A consistently high value of $R^2$(>0.75) demonstrate the applicability of our empirical model.

electronic contribution to thermal conductivity is well described by the Wiedemann-Franz law in metals[5] for free electrons and the lattice contribution is well described by Boltzmann transport utilizing the phonon gas approximation for crystalline solids.[6] In polymers and some other amorphous materials, the free electron contribution is negligible and a lattice is ill defined with the lack of regular atomic order (*i.e.,* many polymers are not atomic crystals). Regular atomic order facilitates the definition of a vibration wave-vector and vibration frequency, which constitutes a phonon. Without regular atomic order, the definition of a phonon becomes unclear in amorphous materials. Vibrational modes in amorphous materials can be classified into propagating and non-propagating modes.[3, 8, 9] The propagating modes are similar to phonons as they appear as collective vibrations with long wavelengths and some[3] consider them ballistic vibrations. Allen and Feldman[3] termed these modes propagons (P), whereas the non-propagating modes are further classified into diffusons (D) and locons (L). Locons are localized vibrations and diffusons refer to a diffusive like nature, where the vibrations are neither localized nor propagating. The P-D boundary is termed the Ioffe-Regel crossover and the D-L boundary is termed the mobility edge.

One approach to modeling thermal conductivity that has been applied to amorphous materials is the Einstein model.[11, 12] However, the Einstein model has not been widely adopted because of the ambiguity in choosing a single vibrational frequency and the poor agreement of this model with measured experimental values. An improvement to the Einstein model was suggested by Cahill and Pohl[11] based on the Debye model of vibrations and assuming the lifetime of each oscillator to be half its period of vibration. This has been termed the minimum thermal conductivity or k-min model (for historic reasons as it is not actually a minimum) and is more widely adopted because of its relative good agreement (within an order of magnitude) with room temperature experimental data. As an example, Figure 1c presents the Einstein and k-min predictions for polystyrene along with its measured experimental data.[14] The k-min model gives a good estimate for thermal conductivity at higher temperatures (typically > 50 K) but loses accuracy at lower temperatures. This example of the k-min and Einstein models under predicting the low temperature experimental thermal conductivity data applies to all polymers considered in this study.

Equation (1) is a modified model that accounts for the propagon and diffuson contributions to the thermal conductivity of polymers.

$$k\left(T\right)=f_{\mathrm{P}}\frac{k_{\mathrm{B}}}{v_{\mathrm{s}}}\left(\frac{k_{\mathrm{B}}T}{\hbar}\right)^{1.8}\int_{0}^{x_{\mathrm{P}}}\frac{x^{2.8}e^{x}}{\left(e^{x}-1\right)^{2}}dx+f_{\mathrm{D}}\frac{k_{\mathrm{B}}}{v_{\mathrm{s}}}\left(\frac{k_{\mathrm{B}}T}{\hbar}\right)^{2}\int_{x_{\mathrm{P}}}^{x_{\mathrm{D}}}\frac{x^{3}e^{x}}{\left(e^{x}-1\right)^{2}}dx \qquad (1)$$

The first term on the right-hand side of Eq. (1) is the contribution from propagons and the second term is the contribution from diffusons. This model has only four fitting parameters – the coefficients $f_{\mathrm{P}}$ and $f_{\mathrm{D}}$, and the dimensionless cutoffs $x_{\mathrm{P}}$ and $x_{\mathrm{D}}$ for propagons and diffusons, respectively. Fitting this model to twelve polymers whose temperature dependent thermal conductivity is reported in literature, we find an interesting empirical relationship. The coefficients $f_{\mathrm{P}}$ and $f_{\mathrm{D}}$, have an inverse power-law relationship with the cutoff temperatures $T_{\mathrm{P}}$ and $T_{\mathrm{D}}$, respectively, and a similar relationship is also observed between the coefficients $f_{\mathrm{P}}$ and $f_{\mathrm{D}}$ for propagons and diffusons. Figure 2(a-c) shows the relationship between the fitting parameters, the best-fit equations, and the coefficient of determination ($R^2$) for the inverse power-law fits; Eqs. (2-4) summarize the best-fit inverse power-law equations. The fits for the three equations have coefficient of determination $R^2$ values of 0.81, 0.78 and 0.90, respectively. The cutoff

temperatures, $T_P$ and $T_D$, in these inverse power-law fits are in K, $f_P$ is in $s^{-0.2}$, and $f_D$ is dimensionless.

$$T_P = 53.94 f_P^{-0.278} \quad (2)$$

$$T_D = 72.27 f_D^{-0.283} \quad (3)$$

$$f_D = 25.09 f_P^{-0.768} \quad (4)$$

For our model to be complete, it is necessary to relate at least one of the four variables in the model to fundamental material properties like density $\rho$, molecular weight $M$, and speed of sound $v_s$. For crystalline materials, we can define a Debye temperature using Eq. (5),[11, 14] which is the highest temperature achieved from a single normal vibration.

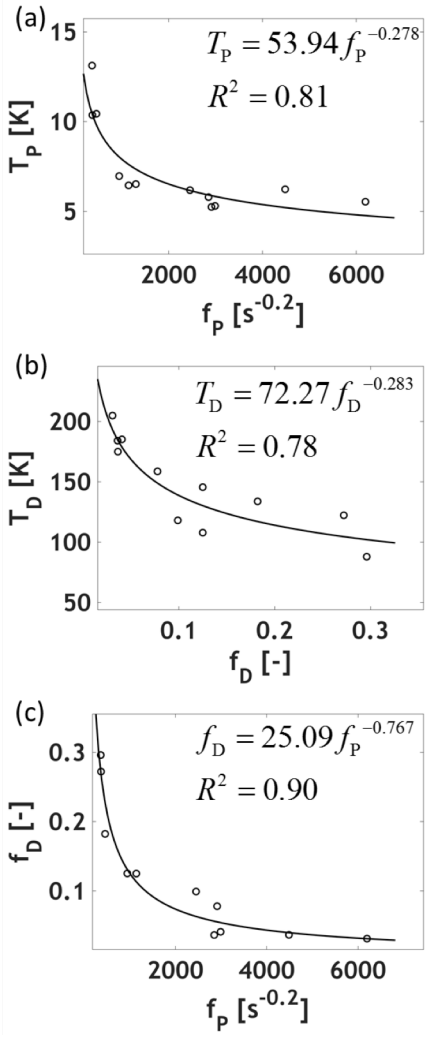


Figure 2. The fitting parameters are plotted against one another highlighting their inverse-power law relation. The best fit is also shown for all plots, along with their equations and $R^2$ values are also shown.

We extend the same definition to polymers and use the monomer molecular weight and the average of longitudinal and transverse modes of the speed of sound for $v_s$. With this modified definition of a Debye temperature, we relate the diffuson cutoff temperature $T_D$ to $T_{Deb}$ (in [K]) and $\rho$ (in [kg·m$^{-3}$]) using an inverse power law-fit that has an $R^2$ of 0.84 given in Eq. (6) shown in Fig. 3.

$$T_{\mathrm{Deb}} = v_{\mathrm{s}} \frac{\hbar}{k_{\mathrm{B}}} \left(6\pi^2 n\right)^{1/3} \tag{5}$$

$$T_{\mathrm{D}} = 1.465 \times 10^{7} \left(\rho \sqrt{T_{\mathrm{Deb}}}\right)^{-1.23} \tag{6}$$

This simple empirical model is useful because it (i) allows for facile estimation of the temperature dependent thermal conductivity, and (ii) quantifies the number and contributions of propogating and diffusive thermal modes in polymers. How these vibrational modes couple to electronic and thermoelectric transport is one of the next steps that we plan to investigate. Finally, based on this model, it also predicts an upper limit to the thermal conductivity of polymers given as:

$$k_{\max} = \frac{1}{v_{\mathrm{s}}} \left( 1.036 f_{\mathrm{P}}^{\,0.5} + \frac{2483.3}{f_{\mathrm{P}}^{\,0.33}} \right) \tag{7}$$

It is possible for polymers to have higher thermal conductivity than this limit but that increase would result from the presence of localized vibrational modes (i.e., vibrons). Deeper investigation into the implications of this maximum limit need to be performed.

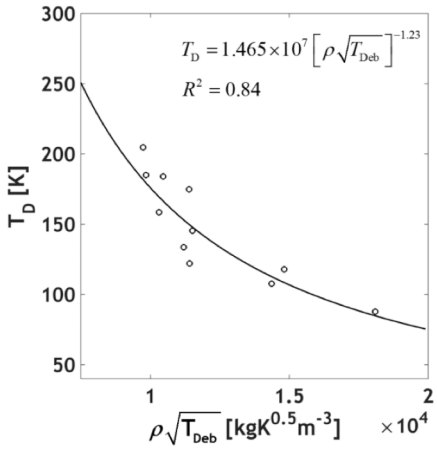


Figure 3. The diffuson cutoff temperature ($T_D$) is plotted as a function of density and Debye temperature highlighting the inverse power-law relation. The best least squares fit is also shown, along with its equation and $R^2$ value.

## New Thermal Measurement Technique for Anisotropic Materials

### *Photothermal Technique*

We have also finished a new thermal measurement technique that is capable of simultaneously measuring the through-plane and in-plane thermal conductivity to a high degree of certainty. We refer to this technique as Beam-offset Frequency Domain Thermoreflectance (Beam-offset FDTR). This is a different realization than the Broad-Band FDTR that was discussed in the previous year. This technique is useful for measuring the thermal conductivity of polymer and higher thermal conductivity multifunctional materials.

Beam-offset FDTR is a pump-probe thermoreflectance technique that uses a pico-motor mirror to precisely control the location of a probe laser relative to a pump laser. By sweep in space and in heat frequency we can extract through-plane and in-plane thermal conductivity. When these properties are measured using conventional transient thermoreflectance techniques, the accuracy of the $k_{//}$ measurement is dependent on the accuracy of measuring $k_{\perp}$, and vice versa. This is especially problematic for thin-films measurements as uncertainty in $k_{\perp}$ (~5%) can propagate and grow for uncertainty in $k_{//}$. In the published paper, we present a method for the simultaneous measurement of $k_{\perp}$ and $k_{//}$ using beam-offset FDTR with robust uncertainty estimation. The conventional diffusive heat transfer solution is analyzed to show that offset and heating frequency can independently control the sensitivity to directional thermal conductivity

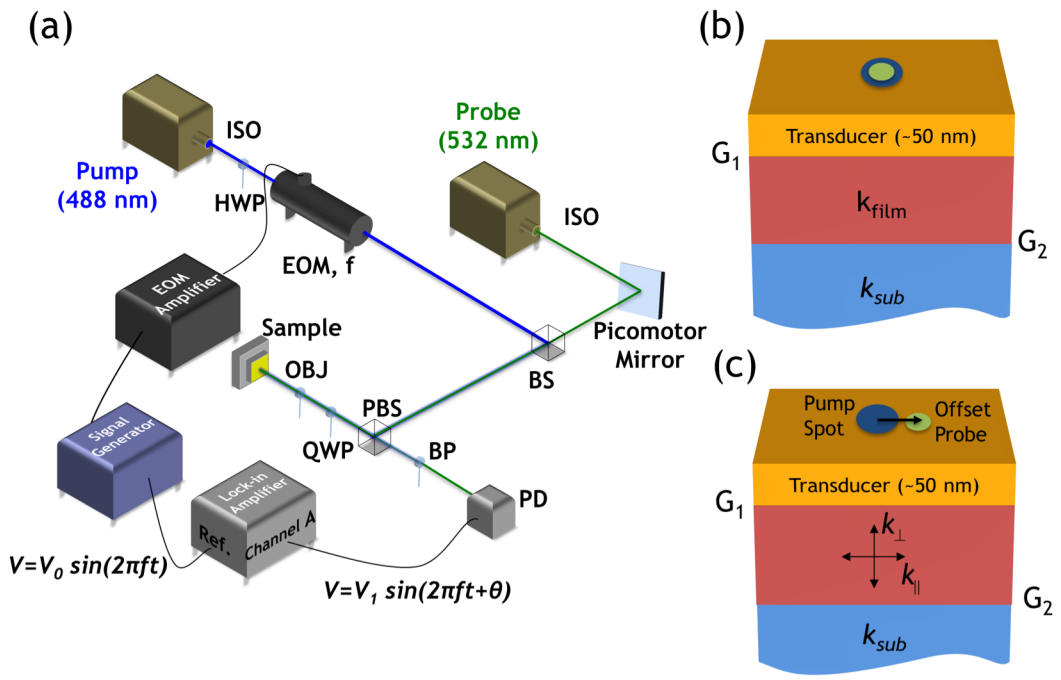


Figure 4. (a) Schematic of an offset FDTR set-up. The only difference between the experimental set-ups of offset FDTR and traditional FDTR is the addition of the picomotor mirror, which scans the probe beam across the sample to create precise offsets between the pump and probe beams. (b) Sample configuration for traditional FDTR. The pump beam (blue) is concentrically aligned with the probe beam (green). The interfacial thermal conductance between the transducer and film is labeled $G_1$ and the conductance between the film and substrate is labeled $G_2$. (b) Sample configuration for offset FDTR. The probe beam is offset from the pump beam and the film or substrate may have unique values for through-plane ($k_{\perp}$) and in-plane ($k_{||}$) thermal conductivity.

Table 1. Literature and measured values for in-plane thermal conductivity ($k_{\parallel}$), through-plane thermal conductivity ($k_{\perp}$), and volumetric heat capacity ($C_v$) and measured values for thermal interface conductance ($G_1$ and $G_2$ for a-$Al_2O_3$).

| | Literature | | | Measured (this work) | | |
|---|---|---|---|---|---|---|
| Sample | $C_v$(MJ/m$^3$-K) | $k_{\perp}$(W/m-K) | $k_{\parallel}$(W/m-K) | $k_{\perp}$(W/m-K) | $k_{\parallel}$(W/m-K) | $G$(W/m$^2$-K) |
| Fused Silica | 1.6 ± 0.1[2] | 1.4 ± 0.1[2] | 1.4 ± 0.1[2] | 1.3 ± 0.5 | 4.6 ± 4.6 | 70±23 |
| Quartz | 2.0 ± 0.2[2] | 5.9 ± 0.9[2] | 11.0 ± 1.0[2] | 6.3 ± 1.2 | 10.3 ± 3.0 | 51±11 |
| a-$Al_2O_3$ | 3.2 ± 0.3[4] | 0.8 ± 0.2[4] | 0.8 ± 0.2[4] | 0.9 ± 0.4 | 2.6 ± 2.6 | 71±16, 68±24 |
| c-$Al_2O_3$ | 3.2 ± 0.3[7] | 25 ± 3[7] | 33 ± 4[7] | 25.5 ± 2.5 | 37.6 ± 7.0 | 390±56 |
| HOPG | 1.6 ± 0.1[10] | 8 ± 2[10] | 1800 ± 200[10, 13] | 9±2.7 | 1861±744 | 104±43 |

and extract values for $k_{//}$ and $k_{\perp}$. Numerical uncertainty analyses demonstrate that sweeping both heating frequency and beam offset results in a reduction of measurement uncertainty. This modified measurement technique is demonstrated on crystalline alumina (c-$Al_2O_3$), amorphous alumina (a-$Al_2O_3$), quartz, fused silica, and highly-oriented pyrolytic graphite (HOPG).

Measurement capabilities have been demonstrated over a range of thermal conductivities (~1-2000 W/m-K) and materials ranging from isotropic ($k_{\parallel}/k_{\perp}$=1) to highly anisotropic ($k_{\parallel}/k_{\perp}$>300) with a reduced in-plane measurement uncertainty compared to alternative FDTR approaches.[30] Measurement uncertainty for through-plane thermal conductivity ranged between 10-45% with uncertainty increasing as thermal conductivity decreased. Measurement uncertainty in the in-plane thermal conductivity varied between 10-20% for materials with conductivities greater than 5 W/m-K. However, uncertainties are larger for in-plane thermal conductivity below 5 W/m-K because of lateral heat spreading in the Au transducer. Despite its high in-plane conductivity, measurement uncertainty for in-plane thermal conductivity of HOPG approached 40% due to uncertainty in the transducer thickness.

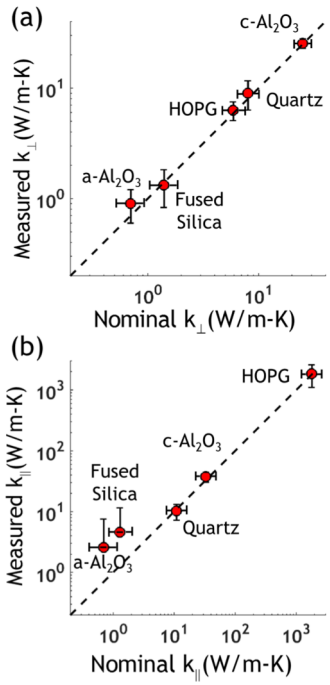


Figure 5. **(a) Comparison between measured and nominal values for $k_{//}$. Vertical error bars indicate measurement uncertainty and horizontal bars indicate uncertainty in nominal value. (b) Comparison between measured and nominal values for $k_{\perp}$.**

***Electrothermal Technique***

Anisotropic thermal conductivity can complicate the performance of semiconducting polymer thin-films in applications such as thermoelectrics and photovoltaics. Anisotropic measurements of low thermal conductivity polymers are challenging and there are a limited number of appropriate measurement techniques. Suspended film 3-omega is an appropriate technique but has often re-quired unfavorable microfabrication. Herein, we report on the utility of the suspended 3-omega technique that uses shadow mask-ing, and no other microfabrication techniques, in performing anisotropic (in-plane and through-plane) thermal conductivity meas-urements of N2200 and a low molecular weight P3HT, which are two common n-type and p-type semiconducting polymers. We fur-ther report on the necessary conditions for the validity of the 1D suspended film heat transfer model and provide experimental guidelines for in-plane thermal conductivity measurements of polymer thin-films. Measured thermal conductivities are compared with predictions from the conventional k-min model and a recent empirical model that more accurately predicts the temperature dependence.

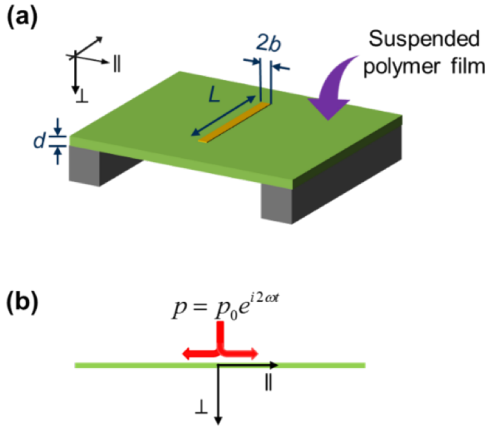


Figure 6. (a) Configuration of the suspended film and metal heater-line for in-plane measurements. (b) Heat flow configuration used in the 1D analysis. The in-plane and through-plane directions are shown.

3ω is a commonly used electro-thermal technique to measure thermal conductivity of thin-films due to the technique's high degree of accuracy, and can be modified to measure the thermal conductivity of polymer films. In a conventional 3ω measurement, an electrical current at an angular frequency $\omega$ (=$2\pi f$) is sourced through a metal heater line deposited atop a thin-film. This results in periodic Joule heating of the line heater at a frequency $2\omega$, which creates a thermal wave that penetrates the sample. The amplitude of the temperature oscillation of the heater depends on the thermal properties of the thin-film. The periodic temperature oscillation follows the heating and occurs at a frequency $2\omega$, but is delayed in phase $\phi$ (*i.e.*, the phase lag). This temperature oscillation then causes the resistance of the heater to oscillate at $2\omega$. A voltage at $3\omega$ results because the current is sourced at a frequency $\omega$ and the resistance changes at a frequency $2\omega$; this $3\omega$ voltage can be used to extract thermal properties. While traditional 3ω methods and analyses were developed for isotropic samples, there have only been a few modifications to characterize anisotropy. These modifications involve sample-heater configurations, such as a film on a substrate with heater widths comparable to film thickness,[15-17] suspended film with a metal heater,[18, 19] heat spreader method,[20, 21] and electrically conductive suspended films in a self-heating configuration.[22, 23] Additionally, film-on-substrate configurations typically require complicated microfabrication and prior knowledge of through-plane conductivity. Alternatively, the suspended film configurations (both the external heater and self-heating variants) has the advantage of obtaining in-plane thermal conductivity without exact knowledge of the through-plane conductivity.

Herein, we focus on the suspended film configuration with a metal line heater atop a polymer thin-film. For thin-films with narrow heater lines, the thermal transport can be approximated using a 1D heat transfer model. While this configuration has been studied previously,[18, 24] they have been limited to very thin-films ($\lesssim$ 1 μm) and heater lines patterned

using lithography were required. Since polymers are often affected by microfabrication solvents, protective layers are often required to protect the films which reduce measurement accuracy. Herein, we explore the limits of a 1D heat transfer model that can be widely applied to measure anisotropic thermal conductivity of polymer films using heater lines deposited through a simple shadow mask, thus eliminating the need for more complicated microfabrication. Sufficient conditions for the validity of 1D model are developed in this letter and are validated against PVDF (a well-characterized isotropic polymer), and muscovite mica (a naturally occurring mineral with a high degree of anisotropy). We then characterize anisotropic thermal conductivities of two prominent semiconducting polymers: commercially available N2200, and a low molecular weight P3HT. The measured thermal conductivities are compared to recent model predictions providing insight into the fundamental thermal transport processes occurring in these common semiconducting polymers.

Figure 6 shows the geometric configuration of the suspended film and the metal heater line that are considered in the suspended film 3ω technique. The generalized solution for a multi-layered system[17] can be simplified to obtain the 2ω temperature rise for a suspended film configuration, and is given by Eq. 1. Here, $b$ is the half-width of the heater line, $d$ is the film thickness, and $p_0$ is the peak power per unit length dissipated by the heater. $k$ and $C$ denote the thermal conductivity and volumetric heat capacity of the film. Volumetric heat capacity is the product of density ($\rho$) and specific heat($c$). $\perp$ and $/\!/$ represent through-plane and in-plane directions, respectively.

$$\Delta T = \frac{p_0}{\pi k_\perp}\int_0^\infty \frac{1}{B\tanh(Bd)}\left(\frac{\sin(b\lambda)}{b\lambda}\right)^2 d\lambda, \quad \text{where } B = \sqrt{\frac{k_{/\!/}}{k_\perp}\lambda^2 + j\frac{2\omega C}{k_\perp}} \tag{8}$$

The thermal wave at frequency $2\omega$ penetrates the film in $\perp$ and $/\!/$ directions, with the characteristic length scales (*i.e.*, penetration depths) given by Eq. 2. Under negligible film thickness (*i.e.*, $d/L_{p,\perp} \lesssim 0.4$, discussed in greater detail later) and negligible heater width (*i.e.*, $b/L_{p,/\!/} \lesssim 0.4$, discussed in greater detail later) assumptions, the complex temperature rise in the frequency-domain can be simplified to Eq. 3.[18] This solution is independent of the heater line width and the through-plane thermal conductivity. With independent measurements of specific heat (from techniques such as differential scanning calorimetry) and density (from techniques such as volume displacement) to obtain $C$, it is possible to determine the in-plane thermal conductivity directly using the suspended film $3\omega$ technique with only a single metal heater line.

$$L_{p,\perp} = \sqrt{\frac{k_\perp}{2\omega C}}, L_{p,/\!/} = \sqrt{\frac{k_{/\!/}}{2\omega C}} \tag{9}$$

$$\Delta T_{1D} = \frac{p_0}{2d\sqrt{2\omega C k_{/\!/}}} e^{-j\pi/4} \tag{10}$$

Using the suspended 3ω technique, two common semiconducting polymers – N2200 (or P(NDI2OD-T2)),[25] a commercially available n-type semiconducting polymer, and P3HT (Mw ~10532 Da ), a common p-type semiconducting polymer synthesized by Grignard Metathesis method[26] – are thermally characterized. The density of P3HT was determined using water displacement method, while the density of N2200 was indirectly calculated from speed of sound (using picosecond acoustics) and elastic modulus (using nanoindentation) measurements. This approach was adopted due to the limited quantity of material available (<200 mg). Specific heat capacities of P3HT and N2200 were measured using differential scanning calorimetry. In addition to in-plane thermal conductivities, the through-plane values are also measured using the differential 3ω method.[15, 17] Thin-films of P3HT (≈300 nm) and N2200 (≈345 nm) were spun-coat at 1000 rpm for 60 s on a silicon substrate with a 100 nm oxide layer. All measured thermophysical properties are summarized in Table 1. (*Refer to Supporting Information for details on c, ρ and $k_\perp$ measurements.*) The measured thermal conductivity of P3HT is higher than the value reported in literature (~0.18 W/m-K),[27] and we attribute this to orientation of side chains in the low molecular weight P3HT used.

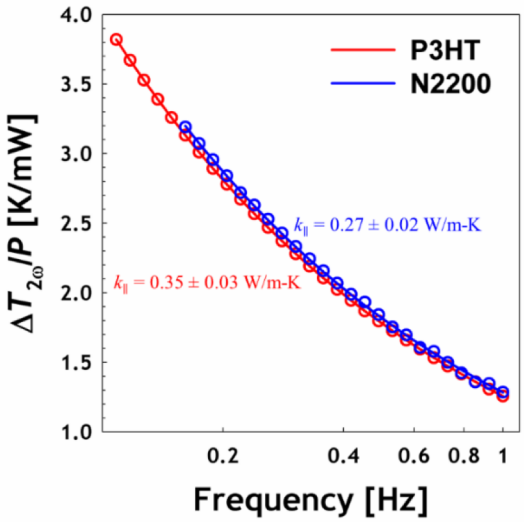


Figure 7. Experimental normalized 2ω temperature amplitude for suspended P3HT and N2200 (open circles), along with the corresponding 1D model fits (solid lines). Dimensions and frequencies are chosen such that $\eta$>0.8.

To obtain suspended films for in-plane measurement, P3HT and N2200 were drop-cast on a silicon substrate to obtain films of thicknesses 35 ± 1.5 and 32 ± 2 μm, respectively. The films were peeled off using water flotation technique, which involves immersing the film-on-substrate in DI water until the film peeled off the substrate (typically within 60 seconds). The films were heated in a vacuum oven at 100 °C to remove residual water from the films. Gold heater lines of $L$ = 4.5 mm and $2b$ = 20 μm were deposited on the film, and frequencies were chosen to satisfy $\eta$ > 0.4. The film was suspended between two Si substrates, and experiments were performed at high vacuum levels (<$10^{-5}$ torr). The results of the 3ω measurements on the suspended film were fit to the 1D model, and the in-plane plane thermal conductivity of P3HT and N2200 were determined to be 0.35 ± 0.03 and 0.27 ± 0.02, respectively. Figure 7 shows the experimental data and the 1D model fits for the suspended films. These values are greater than the through-plane conductivities, resulting in anisotropies ($k_\parallel/k_\perp$) of 1.3 and 1.7 for P3HT and N2200, respectively.

Table 2. Summary of thermal properties of P3HT and N2200.

| Polymer | 3ω measurements | | | Speed of sound | | Density and heat capacity | | | Model predictions | |
|---|---|---|---|---|---|---|---|---|---|---|
| | $k_\perp$ (W/m-K) | $k_\parallel$ (W/m-K) | $k_\parallel/k_\perp$ | $v_{s,T}$ (m/s) | $v_{s,L}$ (m/s) | $\rho$ (g/cc) | c (J/g-K) | $n$ x$10^{22}$ ($cm^{-3}$) | $k_{min,highT}$ (W/m-K) | $k_{emp,max}$ (W/m-K) |
| P3HT | 0.27±0.02 | 0.35±0.03 | 1.30 | 1400 | 2800 | 0.95±0.05 | 1.53±0.08 | 3.51 | 0.38 | 0.25 |
| N2200 | 0.16±0.01 | 0.27±0.02 | 1.69 | 930 | 1860 | 1.32±0.07 | 1.35±0.07 | 4.30 | 0.29 | 0.17 |

The measured thermal conductivities of P3HT and N2200 are compared with the predictions of two models – the minimum thermal conductivity model (k-min)[11] and a recently developed empirical model for polymers.[28] The k-min model is commonly used to predict thermal conductivity of amorphous solids. The empirical model was developed to predict temperature dependent thermal conductivity of amorphous polymers. Both the k-min and empirical model provide (high-temperature) upper-limits to thermal conductivities given by Eqs. 4 and 5, respectively, and can be used to predict room-temperature thermal conductivities of amorphous polymers. Here, $n$ is the number density, and $v_{s,L}$ and $v_{s,T}$ are the longitudinal and transverse values of speed of sound ($v_{s,av}$ is the average of these two values). The number density can be obtained from the measured volumetric heat capacity using the Dulong-Petit limit, $C=3nk_B$, where $k_B$ is the Boltzmann constant.

$$k_{\min,\text{high T}} \approx 0.40 k_B n^{2/3}\left(v_{s,L}+2v_{s,T}\right) \tag{11}$$

$$k_{\text{emp,max}} = \frac{1}{v_{s,av}}\left[\frac{1.43\times10^{13}}{\left(\rho T_{\text{Debye}}\right)^{2.83}} + 5.27\times10^{-6}\left(\rho T_{\text{Debye}}\right)^{1.87}\right] \tag{12}$$

Longitudinal speed of sound ($v_{s,L}$) in N2200 is calculated from picosecond time-resolved acoustic measurements using an optical pump-probe technique on ≈100 nm thick N2200 film on sapphire substrate. The transverse speed of sound ($v_{s,T}$) is assumed to be half the longitudinal value (which is equivalent to assuming a Poisson ratio of 0.33). The speed of sound in P3HT is calculated by measuring its elastic modulus using the nanoindentation technique, and assuming a Poisson ratio of 0.33. The assumption of $v_{s,L}/v_{s,T}$ =2 (equivalent to a Poisson ratio of 0.33) is reasonable with <15% error in most polymers.[29] Thermal conductivity predicted by both models are listed in Table 2, and give reasonable estimates of the thermal conductivity It can be readily observed that the k-min model prediction is closer to the measured in-plane conductivity, and the empirical model is closer to the through-plane conductivity. While this is interesting, no significance can be attributed to this trend since both models assume isotropic material properties.

**New Thermoelectric Device Architectures**

Conducting polymers are a viable option for the thermoelectric generators (TEG) with intrinsic advantages over their inorganic counterparts since they are abundant, flexible as thick-films, and have reduced manufacturing costs due to solution processing. Furthermore, polymers have an inherently low thermal conductivity, thus affording them the option of forgoing some heat exchanger costs. Current examples of polymer TE devices have been limited to traditional flat-plate geometries with power densities on the $\mu W/cm^2$ scale, where their potential is not fully realized. For the first time, we reported a novel radial device architecture and model the improved performance of polymer-based TEG based on this architecture. Our radial architecture accommodates a fluid as the heat source and can operate under natural convection alone due to heat spreading. Analytical heat transfer and electrical models were presented that optimize the device for maximum power density, and for the first time we obtained the geometry matching condition that maximizes the efficiency. We predict high power densities of ~ 1 $mW/cm^2$ using state-of-the-art polymer TEs subjected to a temperature difference of 100 K, which is nearly 1000x higher than polymer flat-plate architectures currently reported in literature.

One of the greatest advantages that a radial architecture facilitates is thermal spreading accommodating natural convective cooling when the thermal conductivity of the active TE material is <0.5 W/m-K. This naturally drives the device architecture to a condition where the conventional fill factor, $F$, is greater than unity. Thus, device and geometry optimizations were revisited and new optimization conditions were achieved (see Table 3). Using these conditions, a high-power density ~1 $mW/cm^2$, which would be three-orders-of-magnitude better than current state-of-the-art (see Fig. 8) radial module can potentially be realized if best-in-class OTE materials can be effectively scaled up and processed.

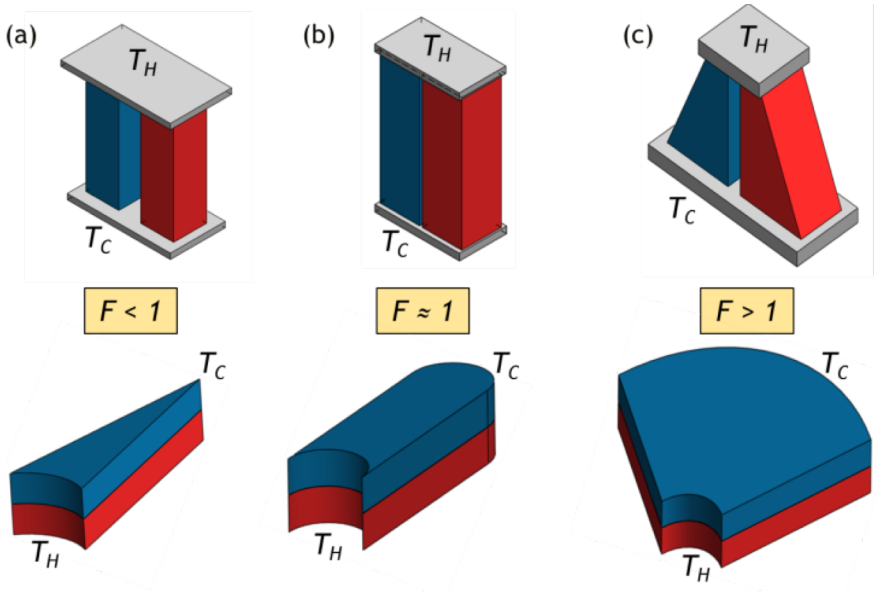


Figure 8: A representation of different fill factors, $F = A_{TE}/A_{HX,H}$ for flat-plate and radial architectures. The n- and p-type active TE material are shown in red and blue, while $T_H$ and $T_C$ correspond to the fixed hot-side and cold-side temperatures. (a) Heat is concentrated when the area of the active TE material is less than the hot-side heat exchanger area resulting in $F < 1$, (b) The fill factor is unity when the areas of the active TE material and hot-side heat exchanger

Table 3. Electrical resistance and thermal conductance equations for a flat-plate and radial TEG. $A_n$ and $A_p$ are the cross-sectional areas of the n- and p-type legs, and $L_n$ and $L_p$ represent their respective leg lengths for a flat-plate device. For the radial device, $r_{out,p}$ and $r_{out,n}$ are the outer radii of the p- and n-type TE material, $r_{in,p}$ and $r_{in,n}$ are the fixed inner radii of the TE material. $\sigma_p$ and $\sigma_n$ are the electrical conductivities. $k_p$ and $k_n$ are the thermal conductivities, and $t_p$ and $t_n$ are the thickness of the TE materials.

| | Flat-plate | Radial |
|---|---|---|
| **Electrical Resistance, $R_{TE}$** | $\frac{L_p}{\sigma_p A_p}+\frac{L_n}{\sigma_n A_n}$ | $\frac{\ln(r_{out,p}/r_{in,p})}{2\pi\sigma_p t_p}+\frac{\ln(r_{out,n}/r_{in,n})}{2\pi\sigma_n t_n}$ |
| **Thermal Conductance, $K_{TE}$** | $\frac{k_p A_p}{L_p}+\frac{k_n A_n}{L_n}$ | $\frac{2\pi k_p t_p}{\ln(r_{out,p}/r_{in,p})}+\frac{2\pi k_n t_n}{\ln(r_{out,n}/r_{in,n})}$ |
| **Geometry Matching Condition** | $\frac{A_n l_p}{A_p l_n}=\sqrt{\frac{k_p\sigma_p}{k_n\sigma_n}}$ | $\frac{t_n\ln(r_{out,p}/r_{in,p})}{t_p\ln(r_{out,n}/r_{in,n})}=\sqrt{\frac{k_p\sigma_p}{k_n\sigma_n}}$ |

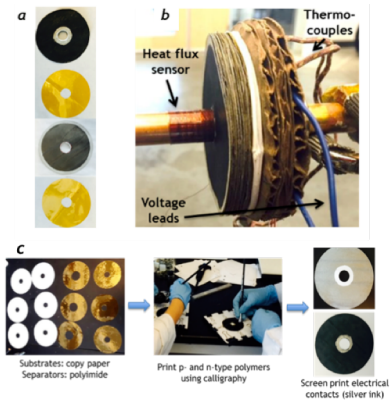


Figure 9: (a) A single p-n couple consisting of an n-type disk, inner separator, p-type disk and and outer separator. (b) Radial TEG experimental setup consisting of 15 p-n couples stacked on a copper rod and cooled by natural convection. (c)Radial TEG step-by-step fabrication process that involves cutting paper disks (substrates) and polyimide disks (separators), coating p- and n-type polymer inks using calligraphy, and screen-printing silver contacts.

With these materials in mind, we were able to demonstrated this radial TEG proof-of-concept made from best-in-class conducting polymers supported on paper substrates. We had to use paper substrates because processing of free-standing thin-film organic thermoelectric materials proved challenging with currently available polymer thermoelectric materials. For the device we report the pristine thermoelectric properties of thin-films of p-type PEDOT:PSS with Te nanowires and n-type poly[$K_x$(Ni-ett)] blended with PVDF/DMSO, as well as the composite properties of these materials on paper. To-date we have been able to synthesize metal-ethylene tetrathiolates (M-ETTs). We have confined our focus to Ni as the metal source because it produces n-type behavior. Through synthetic investigation and optimization, we have been able to fabricate a high conductivity n-type, which we intend to blend and process to further tune the parameters. The performance of this material is summarized in Table 4. Clearly using paper as the substrate effectively makes a composite and reduces the material performance significantly.

Ultimately, we were able to demonstrate the first prototypical device in radial architecture operating under natural convection alone. The prototype device schematic is shown in Fig. 9 and photographs of the assembly process and cross sectional views are shown in Fig. 10. This generator was made from metal coordinated compounds as discussed previously.

Table 4. Thermoelectric properties of polymer thin films and polymer-paper composite at room temp (~ 295 K). "On paper" electrical conductivity values are determined at a thickness = 80 µm

| | $S$ (µV/K) | $\sigma$ (S/cm) | $S^2\sigma$ (µW/m-K²) |
|---|---|---|---|
| p-type PEDOT:PSS with Te nanowires | | | |
| Pristine (thin film) | 109.1 ± 8.6 | 4.2 ± 0.5 | 4.9 ± 0.6 |
| On paper | 204.1 ± 19.8 | (4.9 ± 0.6) x $10^{-3}$ | (2.1 ± 0.4) x $10^{-2}$ |
| n-type poly[Kx(Ni-ett)] with PVDF/DMSO | | | |
| Pristine (thin film) | -34.7 ± 3.1 | 12.6 ± 0.7 | 1.5 ± 0.1 |
| On paper | -28.3 ± 1.5 | 0.5 ± 0.06 | (4.1 ± 0.5) x $10^{-2}$ |

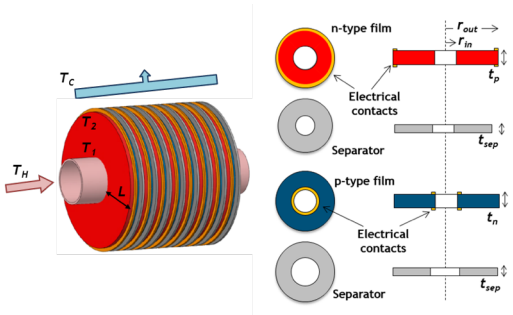


Figure 10: Schematic of a radial TEG where the n- and p-type polymers (shown in red and blue, respectively) coat circular disks. Metal contacts (shown in orange) are used for series connections while separators (shown in gray) electrically isolate adjacent disks. $T_H$ and $T_C$ correspond to the hot and cold-side heat exchanger temperatures, and $T_1$ and $T_2$ are the junction temperatures. $L$ is the leg length, which represents the difference between the outer and inner radii (*i.e.*, $L = r_{out} - r_{in}$), the fill factor is the ratio of the outer and inner radii (*i.e.*, $F > 1$), and $t_p$, $t_n$ and $t_{sub}$ are the thickness of the p-type, n-type, and substrate respectively.

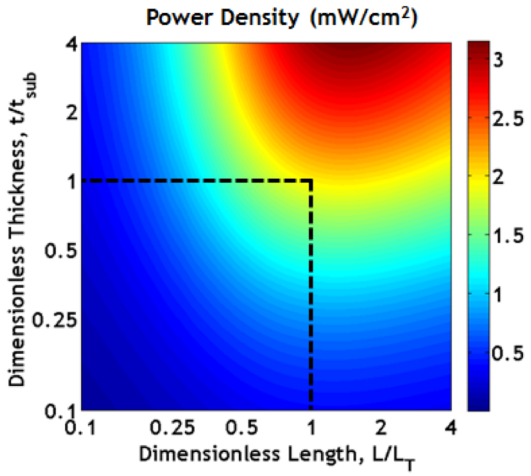


Figure 11: Power density contours as a function of leg length $L = r_{out} - r_{in}$ and active material thickness. The color bar represents the power density values (normalized to the hot-side area). The dashed lines correspond to a power density of 2 mW/cm$^2$ when the leg length is designed at the characteristic thermal length and the TE material thickness is identical to that of the substrate. Example calculation for dedoped PEDOT:PSS when $\Delta T$ = 100 K and the device operates under natural convection alone with $t_{sub}$ = 25 μm, $r_{in}$ = 6.4 mm.

**New Capabilities of OTE Materials by Leveraging Their Unique Processing and Manufacturing Strengths**

Organic materials can be printed into thermoelectric (TE) modules for numerous low temperature energy harvesting applications. The output voltage of printed devices is often limited by (*i*) small temperature differences across the active materials attributed to small leg lengths, and (*ii*) the lower Seebeck coefficient of organic materials compared to their inorganic counterparts. To increase the voltage, a larger number of p- and n-type leg pairs is required for organic TEs; this however results in an increased interconnect resistance, which then limits the device output power. In this work, we discuss practical concepts to address this problem for organic TE modules by printing leg pairs in a hexagonal closed-packed layout. This helps achieve higher fill factors (~91%) than conventional inorganic devices (~25%), which ultimately results in higher voltages and power densities due to lower interconnect resistances. In addition, wiring the TE legs following a Hilbert spacing-filling pattern allows for facile load matching to each application. This is made possible by leveraging the fractal nature of the Hilbert interconnect pattern, resulting in identical sub-modules. Finally, using the Hilbert pattern, sub-modules can better accommodate non-uniform temperature distributions because they naturally self-localize. This opens new avenues for roll-to-roll printing and custom TE module shapes, thereby enabling organic TE modules for self-powered sensors and wearable electronics applications

As a parallel approach to improving material properties (*i.e. zT*) and printability, we explore redesigning the TE module by positioning the legs on a substrate following a different design and connecting them together in a new wiring pattern. Any possible improvements based on this approach can be readily realized in modules that are fabricated using existing TE and interconnect materials.

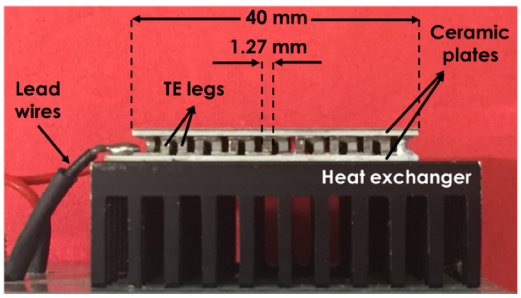


Figure 13. Side view of a commercial inorganic TE device (Custom Thermoelectric, part # 12711-5L30-25CQ) showing p- and n-type legs connected electrically in series. The module consists of 127 p-n leg pairs (254 TE legs) sandwiched between ceramic plates. Device dimensions are provided for FF calculations.

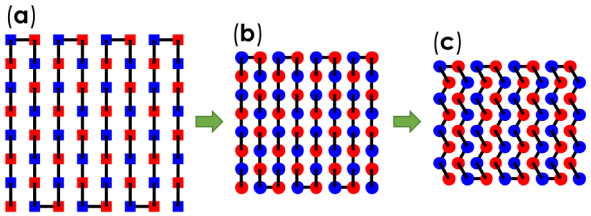


Figure 12. (a) Inorganic fabrication techniques typically produce square cross-section TE legs and use serpentine interconnect patterns. (b) Using high resolution printing, circular cross-sections can be fabricated with legs positioned much closer together, resulting in higher FFs. (c) Even larger FFs can be achieved by placing the legs in a closed-packed structure (hexagonal lattice). The red and blue colors represent p- and n- type materials, respectively.

***Closed-packed layout for larger FFs***

The traditional leg placement and interconnect pattern for a flat-plate $Bi_2Te_3$ thermoelectric module is shown in Fig. 12a. Here, the legs are diced to have rectangular cross-sections, are positioned in a square lattice using a pick-and-place machine, and are wired in series using solder interconnects. Typical leg lengths for these modules are 2-5 mm, and these legs are sandwiched between ceramic plates that serve as the hot- and cold-side heat exchangers. Here, we define FF of a module as the ratio of the area covered by the active TE material to the

hot-side heat exchanger area (this is often the area of the ceramic plates). Based on the dimensions in Fig. 13, the FF for a flat-plate device can be calculated to be ~25%. For organic TE modules, printing-based fabrication techniques allow for a broader range of geometries and interconnect patterns. Particularly, using high resolution inkjet printing, legs with different cross-sections such as circular legs with smaller diameters can be printed much closer together. This results in a higher FF for the module as shown in Fig. 13b, which in turn results in a higher power density for energy harvesting applications. We can take this further and position the legs in a hexagonal closed-packed structure shown in Fig. 13c, which can help achieve a maximum theoretical FF of $\pi/2\sqrt{3}$ ~91% for circular junctions on a two-dimensional plane (see Supplementary Information Note 3). In addition to higher FFs, by placing TE legs closer together, the interconnect length also decreases, which in turn lowers the total resistance and results in a higher power output; this is crucial when the TE module includes a large number of legs (>2000 compared to the typical ~250 legs for inorganic modules).

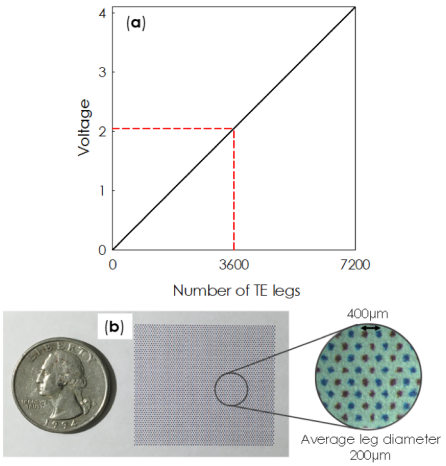


Figure 14. **(a) Output voltage from a module as a function of number of TE legs using properties of dedoped PEDOT:PSS.[1] (b) 3600 legs are positioned in an area of 36.0 mm by 31.2 mm using a desktop inkjet printer (EPSON XP860) to show large FF. Red and blue colors are regular printing inks that represent n- and p-type polymers, respectively, for illustration purposes to distinguish - and p**

To assess the increase in power density that can be obtained using this closed-packed layout of TE legs and to obtain the optimum leg length, we have developed a numerical model that includes material properties, device geometry and thermoelectric effects. As an illustration, we use properties of dedoped PEDOT:PSS[1] ($S$ = 72 μV/K, $\sigma$ = 890 S/cm, and $k$ = 0.33) as the p-type material, and a fictitious n-type material with identical properties except for the sign of the Seebeck coefficient. We model flexible modules by using Kapton films instead of ceramic plates in traditional flat plate devices. For fixed hot- and cold-side temperatures of $T_H$ = 400 K and $T_C$ = 300 K (typical for low grade heat recovery), a system of coupled non-linear equations that includes the Peltier effect and Joule heating terms can be solved numerically.[30-32] The leg length is a design variable that optimizes device geometry and performance. We observe that power density (normalized to the heat exchanger area) increases with leg length, reaches a maximum value called the optimum leg length, and then decreases. This is expected as the thermal and electrical resistances dominate at large leg lengths, thereby reducing the heat through the device and consequently, the power output. As was mentioned previously, the optimum leg length is found to be around 250 μm, and a power density of over 100 mW/cm$^2$ is obtained at this optimized leg length. This is significantly higher than existing organic TEG prototypes indicating that printing closed-packed devices could be very beneficial for achieving high performance. We note here that this is an upper limit on performance since the fill factor that is practically achievable is dictated by the printing method.

***Fractal geometries for interconnect patterns***

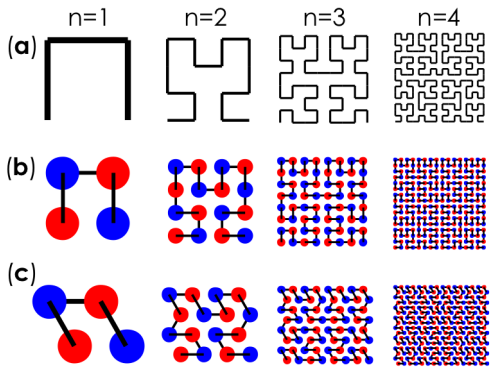


Figure 15. (a) From left to right - Hilbert curves of order one, two, three, and four, which have 4, 16, 64, and 256 legs respectively. (b) Hilbert interconnect patterns can be used to connect TE legs electrically in series where red and blue circles represent n- and p-type materials, respectively. (c) TE legs that are connected by Hilbert curve can also be arranged in a hexagonal closed-packed layout, thus increasing the FFs.

We have shown that using printing techniques, organic TE legs can be positioned closer to each other and in a hexagonal layout to increase power density. We can also print new patterns for interconnects between the legs. A group of patterns that can potentially be utilized as interconnects are fractal geometries with self-similarity characteristics that are referred to as space filling curves. Mathematically, space filling curves are defined as mapping functions from points on a unit interval of [0, 1] to the entire two-dimensional unit square. Hilbert curves and Peano curves are two examples of space filling curves. Recently, Fan *et al.*[33] have shown that these curves provide ideal surface conformations for stretchable electronics. In this work, we choose Hilbert curves for wiring the module, as they not only allow for good surface conformation (which is beneficial for wearable devices),[33] but also self-localize (which is beneficial for maintaining a uniform temperature across all the TE legs). A Hilbert curve of order *n* describes how $4^n$ points are connected as shown in Fig. 15a. To fabricate a TE module, legs can be positioned in place of these points and they can be wired together based on the Hilbert pattern shown in Fig. 15b. Moreover, a hexagonal layout for positioning TE legs can also accompany the Hilbert curve interconnects, thus allowing for much higher FFs, as shown in Fig. 15c.

***Benefits of Hilbert interconnect pattern for printed TE modules***

One major benefit of using space filling curves for wiring interconnects in TE modules is that they allow the module to be divided into fractal geometries or sub-modules. Although in theory all space filling curves allow for dividing into sub-modules, the geometry of the resulting sub-modules differ and are dependent on the chosen curve. For instance, following the Hilbert pattern, we can divide the module into *M* groups of identical parts (*i.e.*, sub-modules) connected in parallel, and each consisting of *N* legs wired in series (*i.e., M*x*N* total number of legs), as discussed below.

***Improved load matching conditions***

A module containing 1024 legs wired together by an order five Hilbert curve can be divided into eleven combinations of *M* and *N* (denoted by (M,N)), as (1,1024), (2,512), (4,256), (8,128), (16,64), (32,32), (64,16), (128,8), (256,4), (512,2), and (1024,1); four of these combinations. Following the concept of tessellating a device into sub-modules, an initial module can be printed such that all legs are connected in series (*i.e.,* (1, *M*x*N*) combination), and then based on the end application, it can be divided into a desired number of sub-modules connected in parallel. This opens up avenues to tailor the module such that it is electrically impedance matched or load matched to the application; electrical impedance matching[30, 32, 34] is essential to obtain maximum power from the module. This is a significant advantage for printable TE and a key outcome of this work, as these modules are no longer reliant on power conditioning circuits (*e.g.*, DC-DC converters or boost converters) to match the impedance of the module to the application.

We extend these wiring rules and interconnect patterns for closed-packed configurations with a large number of legs, as would be the case for organic devices. For this, we define a cell based on a four-leg basis (two p-type legs and two n-type legs) rather than the traditional two-leg basis that is widely used for TE devices. Using this basis, there are four possible unique arrangements of these closed-packed legs, resulting in four types of cells as shown in Fig. 16a. We restrict the total number of cells in a module to being a power of four, resulting in a total number of legs of $4^n$ where $n$ is the order of the Hilbert curve (*e.g.*, $n$ = 1,2,3,…). This allows us to connect adjacent cells rather than individual legs using a Hilbert curve. From a macroscopic perspective, the legs placement pattern appears more random than the traditional serpentine alternating p-n placement used widely, but it does contain deeper order. As an illustration in Fig. 15b, we use a Hilbert curve of order 2 to connect 16 cells comprising 64 TE legs in total. The voltage output from this configuration is $V=N(2S_{pn})\Delta T$ using the four-leg basis. For a larger number of legs, we can tessellate the module into *N* cells connected in series and *M* groups connected in parallel for load matching as we discussed previously. Figure 16c shows this module configuration for an electrically impedance matched device for various combinations of *M* and *N* achieving the requisite load matching.

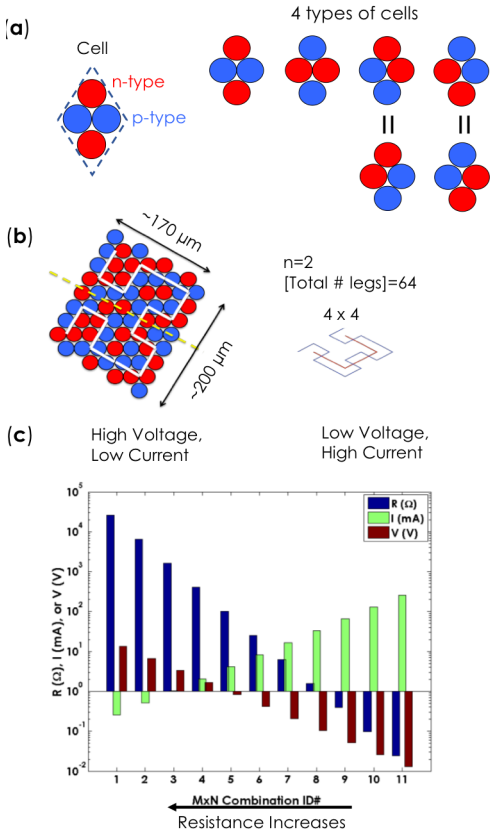


Figure 16. (a) A four-leg basis consisting of two n-type and two p-type legs closed-packed to form a cell, and the four resulting unique cell configurations, (b) a Hilbert curve of order two connecting eight cells in series to form a TE module, and (c) various combinations of *N* cells in series and *M* groups in parallel for load matching to a range of applications. *M*x*N* combination ID#s from 1 to 11 refer to the following (*M*,*N*) designators, respectively: (1,1024), (2,512), (4,256), (8,128), (16,64), (32,32), (64,16), (128,8), (256,4), (512,2), and (1024,1).

**Improve the Performance of Pre-Existing Best-In-Class OTE Materials by Strategically and Rationally Modifying their Chemistry, Structure, and Processing Conditions.**

Nickel ethenetetrathiolate (NiETT) coordination polymers have been shown to exhibit high thermoelectric performance as pressed pellets. Since the material is insoluble, films are formed by fabricating a composite of the material in an inert polymer matrix, a process which adversely impacts thermoelectric properties. To date, a reliable and reproducible synthesis has not been reported, which motivated us to undertake a systematic study of the sub-steps involved to understand the reaction mechanism. The results of these studies yielded optimized reaction conditions for high performance n-type films, which were derived from empirical studies and material characterization. Herein, a reaction procedure is presented that gives reproducible properties when preparing batches in the 0.5 to 15-gram range. The identity of the counter ion, nickel equivalency, and oxidation extent are investigated and provide insight into the synthetic reaction mechanism and the ligand-centered oxidation process in these polymers. Optimized materials based on Na[NiETT] exhibit one of the highest *n*-type thermoelectric performance for solution-processed films reported to date, with power factors of 23 μW/m-K$^2$ (due to conductivities approaching 50 S/cm) while maintaining their stability in air.

NiETTs offer advantages in that they: *(i)* have tunable electronic properties through multiple oxidation states on both the ligand and metal center, *(ii)* exhibit n-type behavior as evidenced by their negative Seebeck coefficients, and *(iii)* are stable to ambient conditions without special exclusion of moisture or oxygen. However, NiETTs also have drawbacks associated with their production and processing: *(i)* the poorly understood synthetic pathway leads to irreproducible syntheses, *(ii)* the insoluble nature of the final material limits traditional structural characterization, and *(iii)* fabrication via solution-based techniques requires the use of an insulating matrix that adversely affects performance. Herein, these drawbacks are systematically addressed to provide a deeper understanding of the polymer by developing an optimized synthesis that is reproducible and scalable. As a result, electrical conductivities and thermopower properties are obtained that yield a power factor as high as 23 μW/m-K$^2$, which to our knowledge is one of the highest reported values for a solution-processed air-stable n-type polymer film.[36-40] Moreover, the synthetic variability inherent in these systems allows for tuning $S$ and $\sigma$ to achieve desired performance.

***Enhancing Na[NiETT] Thermoelectric Performance***

The poorly understood reaction mechanism in the formation of NiETT and lack of characterization techniques available for studying the structures of these insoluble complexes make synthetic optimizations difficult. To better understand how changes to the reaction conditions affect thermoelectric performance, the reaction is sub-divided into three major steps (Figure 17). Systematic variations across individual steps, while keeping all other reaction conditions constant, create families of materials for direct comparison.

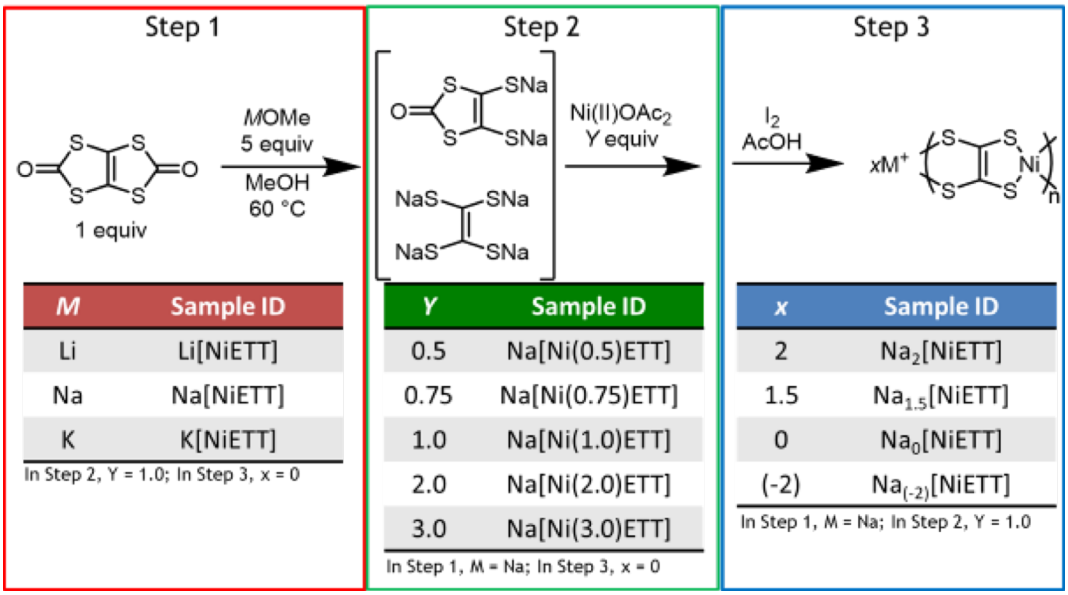


Figure 17. The synthesis of NiETT is sub-divided into three modifiable steps for systematic thermoelectric property optimization.

A rigorous account of all synthetic procedures is provided in the SI, from which certain reaction conditions are found to be critically important to thermoelectric performance, while others have only a minor effect. The refined procedure yields a consistent NiETT material (quantified by elemental composition, XPS, and thermoelectric performance) across multiple batches synthesized at the 500 mg scale, 2 g scale, and 15 g scale.

In Step 1, to isolate the effect of the counter ion on the reaction and final material, three methoxide species were used: lithium methoxide, sodium methoxide, and potassium methoxide. The three otherwise identical reactions yield Li[NiETT], Na[NiETT], and K[NiETT]. In Step 2, to isolate the effect of nickel deficiency or excess, five NiETTs with different equivalents of nickel(II) acetate were synthesized while keeping the counter ion fixed using sodium methoxide: Na[Ni(0.5)ETT], Na[Ni(0.75)ETT], Na[Ni(1.0)ETT], Na[Ni(2.0)ETT], and Na[Ni(3.0)ETT]. Finally in Step 3, to isolate the effect of oxidation extent, four reactions using one equivalent of nickel(II) acetate and sodium methoxide were synthesized: no chemical oxidation, $Na_2$[NiETT]; partial chemical oxidation, $Na_{1.5}$[NiETT]; full oxidation to the neutral polymer, $Na_0$[NiETT]; and over-oxidation, $Na_{-2}$[NiETT]. It has been previously shown that the extent of oxidation from exposure to air drastically affects thermoelectric performance;[41] this is addressed by using a chemical oxidant, *i.e.,* iodine, as control over atmospheric oxidation is challenging. Here, the sodium subscript indicates the expected number of counter ions per repeat unit, and therefore the expected negative charge on the backbone per repeat unit of the polymer. The subscripts on sodium are used exclusively as a naming convention to indicate how the sample was prepared and do not indicate the actual amount of counter ions per repeat unit. The negative subscript indicates a stoichiometric excess of oxidant was used resulting in a hypothetical charge of positive two on the backbone repeat unit; however, in practice with iodine, the oxidation stops at a neutrally charged backbone.

Two qualitatively distinct forms of NiETT are observed across all syntheses: amorphous black powders and blue-gray particles that have reflective facets, indicating the formation of a poly-crystalline or heterogeneous material in contrast to the completely amorphous polymer reported in literature.[42] The elemental composition of both forms are identical, indicating that the effect is morphological and can be attributed to different crystallite sizes or packing differences (Fig. 18c). To understand the synthetic variations and their effect on thermoelectric properties, XPS wass employed to gain insight into the binding environment and material composition. In order to measure the thermoelectric properties of ETT materials, a composite film was fabricated by ball-milling ETT powder with a PVDF matrix to form a dispersion in DMSO. Binder selection and ETT/PVDF ratios were optimized in a prior work and omitted here for sake of brevity.[41]

Annealing the film simultaneously improves the thermoelectric properties, and the results are consistent acorss multiple batches of material (Figure 19). All values reported in this work are for films that were annealed in air at 160 °C for one hour as these conditions provide the highest thermoelectric properties. Annealing results in a 5% mass loss of the ETT powder and a 7% mass loss in the ETT/PVDF film as evidenced from thermogravimetric analysis. It is hypothesized that annealing removes residual DMSO and dehydrates the polymer, while allowing for enhanced electronic coupling between ETT chains as the process is done near the melting temperature of PVDF. A detailed investigation of the effects of annealing on NiETT composites will be reported in a subsequent manuscript, as the focus of this manuscript is the synthetic modifications that enhance thermoelectric performance.

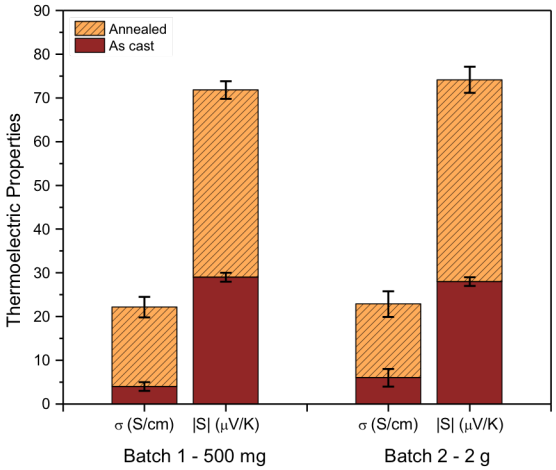


Figure 19. Thermoelectric performance of two batches of $Na_0$[Ni(1.0)ETT] showing consistent performance both before and after film annealing at 160 °C. The Seebeck coefficients of all NiETTs are negative, but the absolute value is shown for simplicity.

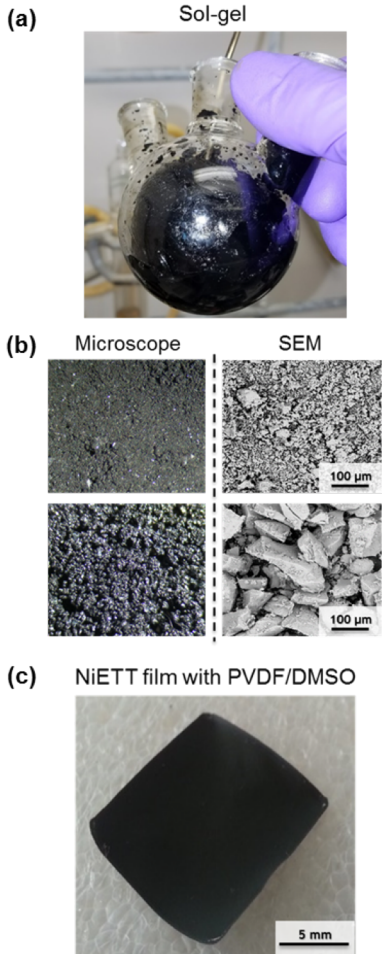


Figure 18. (a) A 100 mL flask containing oxidized Na[NiETT]; (b) Optical microscope (left column) and SEM images (right column) of the two observed forms of NiETT powders: black and amorphous (top row), blue-gray and poly-crystalline (bottom row); (c) Image of fabricated NiETT/PVDF composite film for thermoelectric property measurements.

***The Effect of Synthetic Modifications***

***I. Changing the Counter Ion***

The choice of (*i*) alkali counter ion, (*ii*) nickel stoichiometric equivalents, and the (*iii*) extent of oxidation all impact thermoelectric performance. First, we examine the effect of changing the counter ion; it is well-known that bulky counter ions such as tetraethylammounium can reside between polymer chains and impede charge transport. Alkali counter ions are preferred as their small size allows for close-packing of the polymer chains, thereby facilitating interchain interactions.[42, 43]

The thermoelectric properties of NiETT can be tuned by changing the counter ion (Figure 17). The thermopower of all three variants is negative, confirming that n-type electrical transport is dominant. Interestingly, the electrical conductivity increases and the thermopower decreases by reducing the size of the counter ion; Li[NiETT] with the smallest counter ion has the highest conductivity of 37 ± 1 S/cm, while K[NiETT] has the highest thermopower of -99 ± 8 μV/K. The power factor is highest for Na[NiETT] films at a value of 13 ± 2 μW/m-K$^2$ due to the combination of a moderate conductivity and Seebeck coefficient (23 ± 1 S/cm and -74 ± 3 μV/K). This is in contrast to what has been reported for ETT pellets where K[NiETT] showed superior thermoelectric properties.[42] These differences can be attributed to the fact that the reactions conditions as well as reactant purity in each step dictate the final material performance. The alkali ion composition is consistent across all syntheses at 0.6-0.8 at. % or one counter ion per 10-15 nickel centers.

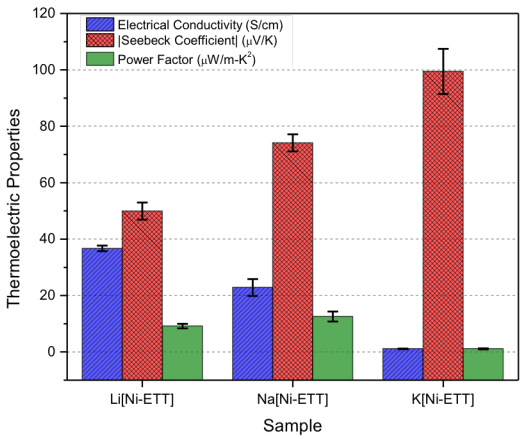


Figure 20. Thermoelectric performance of NiETT with different alkali metal counter ions. Na[NiETT] shows the highest thermoelectric properties with a power factor of 13 μW/m-K$^2$.

The marked difference in thermoelectric performance, despite similar composition and oxidation extent, supports two hypotheses: (*i*) the counter ion affects the reaction pathway and produces a different final material beyond simply exchanging the counter ion; and/or, (*ii*) a property of the counter ion, even at one counter ion per 10-15 nickel centers, directly affects NiETT's intra- and interchain interactions. XPS analysis of sulfur in the three polymers shows different binding environments across the samples; the S2p peak can be deconvoluted into two main binding environments at 161.5 eV and 163.5 eV and the ratio of these peaks differs across all three samples. These differences in the sulfur atoms may affect charge delocalization along the polymer backbone and indicate that the identity of the counter ion plays a role in changing the thermoelectric properties. From the S2p scan, the presence of oxidized sulfur compounds for Li[NiETT] is observed at higher binding energies (~168 eV), that corresponds to an increase in the amount of oxygen in its elemental composition. Ni2p peaks remain unchanged through varying the counter ion, which may be indicative of a ligand-centered oxidation for these complexes that is affected by the identity of the counter ion.[44]

***II. Changing the Equivalents of Ni(II)***

In step 2, the stoichiometric equivalents of the nickel(II) salt were varied using $Na_0$[Ni(1.0)ETT] as the control material to identify the optimum equivalence under these reaction conditions. It has been claimed that excess nickel can produce Ni[NiETT] where it co-acts as a counterion with alkali metals;[42] an alternative hypothesis is that excess nickel acts as a detrimental impurity in the final material. Using anhydrous nickel(II) acetate, which was chosen due to the ease of obtaining the anhydrous salt and its solubility in methanol, removes any uncertainty around the molar mass of the hydrate and the effect on the reaction from hydrated nickel(II) species. The resulting thermoelectric properties (Figure 21) indicate that a power factor enhancement up to 23 μW/m-K$^2$ is achieved by lowering the amount of nickel(II) to 0.75 equivalents.

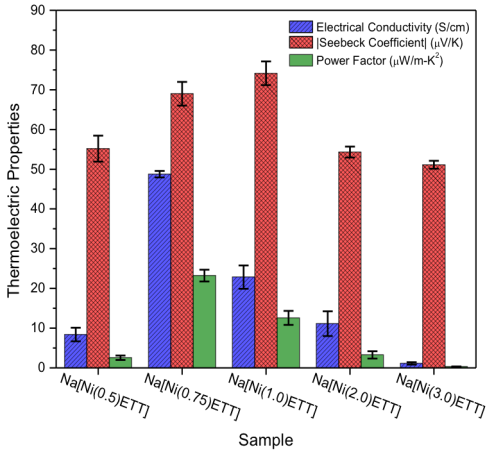


Figure 21. Thermoelectric performance of NiETT with stoichiometric variants of nickel(II) acetate. A sub-stochiometric amount of Ni, *i.e.,* 0.75 equivalents, yields a power factor of 23 μW/m-K$^2$ for Na[NiETT].

To understand the effect of changing the amount of Ni, the % Ni incorporation is calculated in these polymers to quantify how much of the $Ni(OAc)_2$ is present in the NiETT backbone. The higher percent incorporation is found in the sub-stoichiometric nickel equivalents with 80% incorporation for Ni(0.75) compared with 40% incorporation for Ni(2.0). Impurities in the thiapendione (TPD) monomer or degradation during reaction Step 1 is hypothesized to result in less than 100% nickel incorporation, with the optimum level of nickel therefore being sub-stoichiometric. Furthermore, XPS analysis of the Na[NiETT] powders reveals that excess nickel(II), as in the case of Na[Ni(2.0)ETT], forms secondary products that are observed in the Ni and S elemental scans. These impurities are present in lower amounts in the stoichiometric and sub-stoichiometric equivalents.

Given that the overall XPS signal may originate from multiple Ni species in a small binding energy range, the identification of specific compounds is not straightforward. Nonetheless, it is clear that $Ni^{2+}$ is the formal oxidation state across all samples with the peak at 853.4 eV corresponding to the primary Ni-S binding environment. At 855.5 eV, Ni is coordinated with oxygen; the full-width at half-maximum is broad and is attributed to a composite peak of $Ni(OH)_2$ and $NiSO_4$ or other oxidized sulfur species coordinated to nickel (secondary products).[45, 46] This also explains the presence of hydrogen and oxygen in the elemental analysis despite using anhydrous starting materials and working under inert conditions. This is contrary to what has been speculated previously about the peak at 855 eV corresponding to excess nickel acting as a counter ion.[42] Doubling the equivalents of nickel does not lead to the formation of Ni[NiETT] as there is the same atom percent of sodium counter ion present in both Na[Ni(1.0)ETT] and Na[Ni(2.0)ETT]. This may be in part due to the controlled iodine oxidation during reaction Step 3 in this work, thereby eliminating any nickel acting as a counter ion. A low intensity satellite peak ~6 eV to the right of the main peak (~860 eV) confirms that the nickel center exists in a square-planar coordination environment.[47] The ratio of the two Ni peaks changes across the samples – as the equivalents of nickel increases, the peak at 855 eV is intensified, indicating the formation of more secondary products that is consistent with the nickel incorporation amounts presented here. The S2p spectra reveals sulfur in two chemical

environments instead of the single Ni-S-C binding environments that is expected for an infinitely long chain of NiETT. Deconvolution results in peaks at 162 eV and 163.5 eV with the former corresponding to the expected polymer backbone and the latter reflects the influence of ligand acting as end groups.[48] This however suggests a low value for the degree of polymerization for end groups to have a pronounced effect. An alternate explanation for the presence of different sulfur binding environments is the existence of ligand in two different oxidation states, as has been reported for $Ni(dmit)_2$.[49] By changing the nickel(II) equivalents added in the synthesis, the ratio of ligand in these two oxidation states is varied (Figure 20 and Table 5), which in turn affects the thermoelectric properties. A similar observation has been made for p-type CuETTs and confirms a ligand-based oxidation mechanism in these metal-organic complexes.[50] At higher binding energies ~168 eV, there is an additional peak in the S2p spectra which corresponds to oxidized sulfur species such as $SO_x$. This suggests that upon exposure to air before chemical oxidation, some of the Ni-S is oxidized to an oxy-sulfur species in the material as evidenced by the presence of $NiSO_4$ in the Ni2p spectra for all samples.

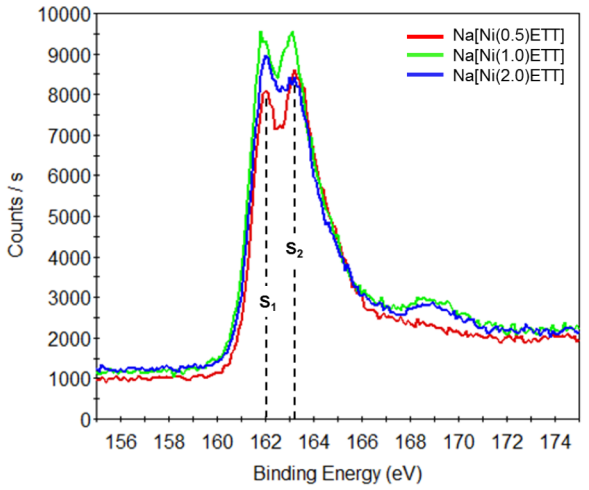


Figure 22. XPS analysis of Na[Ni(Y)ETT] based on different nickel equivalents (Y) showing the presence of three different binding environments for sulfur across all samples.

Table 5. S2p main peak deconvolution into two sub-peaks for different nickel equivalents

| Sample | $S_1$ (162 eV) [Atomic %] | $S_2$ (163.5 eV) [Atomic %] | $S_2/S_1$ |
|---|---|---|---|
| Na[Ni(0.5)ETT] | 51.8 | 37.4 | 0.72 |
| Na[Ni(1.0)ETT] | 54.3 | 33.5 | 0.62 |
| Na[Ni(2.0)ETT] | 57.9 | 29.7 | 0.51 |

### *III. Changing the Extent of Oxidation*

As a final step, the effect of oxidation with iodine was investigated to understand the extent to which thermoelectric properties could be tuned by controlling the oxidation state and thus doping level of the polymer. For this, every attempt was made to prevent the ligand, prepared in situ, from being oxidized until the iodine addition step by handling under an inert atmosphere (argon) using standard Schlenk techniques (see Experimental Section). Most previous literature reports[42, 43] claim the polymer does not precipitate until air is introduced as an oxidant. However, one previous report[51] shows that the polymer precipitates upon addition of the metal salt without any external oxidant. It has also been claimed that even by working under careful anaerobic conditions, there is some unintended oxidation that causes the polymer to precipitate.[52] The observations in this manuscript are contrary to these previous reports, as the reaction intermediately forms a sol-gel (see Figure 18a) during Step 2 of the reaction. Furthermore, from

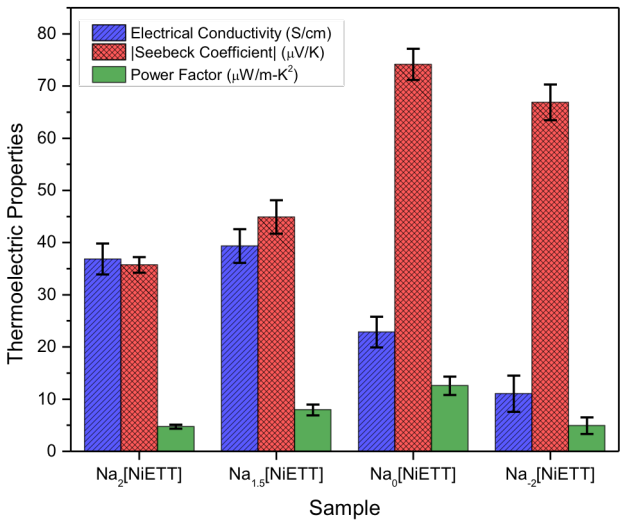


Figure 23. Thermoelectric performance of NiETTs as a function of chemical oxidation equivalents using iodine.

the rigorous air-free reaction conditions employed in our work, observable consumption of iodine during reaction Step 3, and limited oxidized S2p species indicate that unintended oxidation is not the cause of the precipitate or sol-gel formation prior to oxidation. Rather, higher molecular weight species (either branched or linear) are possibly forming in reaction Step 2 and increasing the reaction viscosity. Even without the addition of any iodine, an "unoxidized" polymer is unobtainable as it oxidizes on exposure to air during work-up (filtering and drying) and film fabrication. These workup conditions make $Na_2$[NiETT] (which has no iodine added) an analog to an air-oxidized species moreso than a truly unoxidized polymer. Under these conditions, the electrical conductivity for $Na_2$[NiETT] is 37 ± 3 S/cm while the thermopower shows the lowest value for this family at –36 ± 2 μV/K. The elemental composition shows approximately two sodium atoms per five nickel atoms, indicating a more negative charge on the backbone compared to one sodium atom per ten nickel atoms in the fully oxidized $Na_0$[NiETT]. Upon addition of iodine in Step 3 of the reaction, electrons are extracted from the polymer backbone, which leads to a reduction in electrical conductivity and a simultaneous improvement in the thermopower (Figure 21). This $S$-$\sigma$ tradeoff is analogous to extrinsically doping a polymer and shows that NiETTs can have their oxidation level tuned during synthesis to give desired values for $S$ and $\sigma$.

Given the poor XPS signal-to-noise ratio for $Na_2$[NiETT], it is challenging to extract any noticeable changes in the Ni binding environment. However, a striking difference appears in the S2p spectra between this sample and one that is fully oxidized with iodine. For this "unoxidized" sample, the $SO_x$ peak is more prominent than the main Ni-S peak, which may indicate the formation of more side products. This is also consistent with our previous work on air-oxidized ETTs at short exposure times that yield similar thermoelectric properties.[41] The use of air as an oxidant results in thermoelectric properties of NiETT that vary significantly, and this may explain challenges with material reproducibility in literature. The use of iodine provides greater control of the oxidation step and aloows for some level of tunability in the thermoelectric properties; other oxidizing agents in future studies may enable greater tunability to provide insight into the charge transport in these materials. The iterative refinement of the NiETT synthesis presented in this work avoids batch-to-batch variations and results in a repeatable, high n-type power factor for NiETT/PVDF composites that can be printed into thermoelectric devices and operated in air

**Demonstrate How Electron-Phonon Coupling in Organic and Organic-Inorganic Hybrid/Composite Materials Breaks Fundamental Correlations in Thermoelectric Transport Properties and Leads to New Transport Paradigms.**

Nickel ethenetetrathiolate (NiETT) polymers are promising n-type thermoelectric materials, but their insolubility requires the use of an inert polymer matrix to form films, which is detrimental to the thermoelectric performance. In this work, the use of thermal annealing as a post-treatment process simultaneously enhances the electrical conductivity from 6 ± 2 to 23 ± 3 S/cm and thermopower from -28 ± 3 to -74 ± 4 μV/K for NiETT/PVDF composite films. Spectroscopic characterization reveals that the underlying mechanism involves removal of residual solvent and volatile impurities (carbonyl sulfide and water) in the material, with no measured change in the oxidation level of the polymer backbone. Additionally, microscopic characterization reveals morphological changes caused by a densification of the film that improves chain packing. These effects result in a 25x improvement in power factor from 0.5 to 13.5 μW/m-K$^2$ for NiETT/PVDF films and provides crucial insight into the composition of these coordination polymers.

Metal coordination compounds, specifically metal-dithiolene coordination polymers, consisting of bridging ethentetrathiolate ligands and nickel metal centers (NiETT), are one of the best performing n-type organic thermoelectric materials. Pressed pellets of poly[K(NiETT)] have demonstrated high thermoelectric properties with $S$ = -120 μV/K, and $\sigma$ = 44 S/cm at room temperature, but the insoluble nature of the material limits its applicability.[42] One route to make NiETTs solution processable is by blending it with an inert matrix (*e.g.*, polyvinylidene fluoride or PVDF) and casting from low vapor pressure solvents (*e.g.,* dimethyl sulfoxide or DMSO) albeit at the sacrifice of electrical conductivity.[53] Other strategies include fabricating composites with carbon nanotubes that yield high power factors but the resulting material is often p-type.[54, 55] This indicates the need for studying NiETTs further and developing an n-type material that is high performing and solution processable. We have recently reported an optimized synthesis of Na[NiETT] that provides a reproducible material as validated by elemental analysis, X-ray photoelectron spectroscopy, and consistent thermoelectric properties across batches.[56] In that study, it was observed that annealing composite films of ETT with PVDF/DMSO resulted in a simultaneous increase in $\sigma$ and $S$, thereby yielding power factors over 20 μW/m-K$^2$; this represents a significant improvement over previous reports which had a power factor of 0.4 μW/m-K$^2$ for these same blends.[57] Herein, we elucidate on mechanisms that occur during annealing these films that results in the simultaneously improvement of $\sigma$ and $S$. Specifically, important morphological and chemical compositional changes are induced by annealing at 160 °C. This observation also provides insight into the behavior and composition of these metal coordination polymers. The effects of annealing NiETT have not been reported before, and these results suggest a novel pathway to increase the thermoelectric power factor of metal-coordination polymers

***Processing films of NiETT***

We refer the reader to our previous work on ETT optimization to obtain details on the synthesis parameters and reaction conditions.[56] At the end of the synthesis, the reaction solution is vacuum filtered and dried under vacuum at room temperature for 24 hours to obtain NiETT particles in the form of a blue-gray lustrous powder. Due to the insoluble nature of NiETT, films are fabricated by dispersing the particles in a 10 mg/mL solution of PVDF dissolved in DMSO.

This mixture was then drop cast on glass substrates and dried under vacuum for 30 minutes at 50 $^0$C to remove solvent resulting in films that are 5-10 µm thick. This binder and solvent system is best suited for the formation of continuous composite films by drop casting.[41] The films were subjected to an annealing post-treatment process in air on a hot-plate. To establish ideal annealing conditions, the temperature was varied for NiETT/PVDF films from 80 °C to 160 °C.

*Annealing enhances thermoelectric properties*

The electrical conductivity and thermopower of composite films increase simultaneously with increasing annealing temperature up to 160 $^0$C (Figure 24). Annealing at higher temperatures resulted in severe cracking of films and delamination from the substrate in many cases. The binder and film forming polymer, PVDF, has a $T_m$ of 169 $^0$C. Near and above this temperature, phase separation between NiETT and PVDF is observed. The conductivity increases from 6 ± 2 S/cm for an as-cast film (control) to 23 ± 3 S/cm upon annealing at 160 $^0$C; this is accompanied by an increase in the Seebeck coefficient as shown in Figure 24 from -28 ± 3 µV/K (sample #1) to -74 ± 4 µV/K (sample #2), to yield a power factor over 10 µW/m-K$^2$ for this n-type composite film. To test for air stability during annealing, additional films were annealed at 160 $^0$C in a vacuum and under nitrogen for one hour – the resulting thermoelectric properties were the same as air annealed samples, suggesting that there is no appreciable degradation or redox activity during the annealing process. Improvement in the electrical conductivity with annealing can be attributed to morphological changes but the simultaneous enhancement in Seebeck is surprising. Thermogravimetric analyses (TGA) show that annealing results in a 5% mass loss in NiETT powder and a 7% mass loss in the NiETT/PVDF film, indicating that different species may be evolved during the annealing process resulting in the enhancement in measured thermoelectric properties.

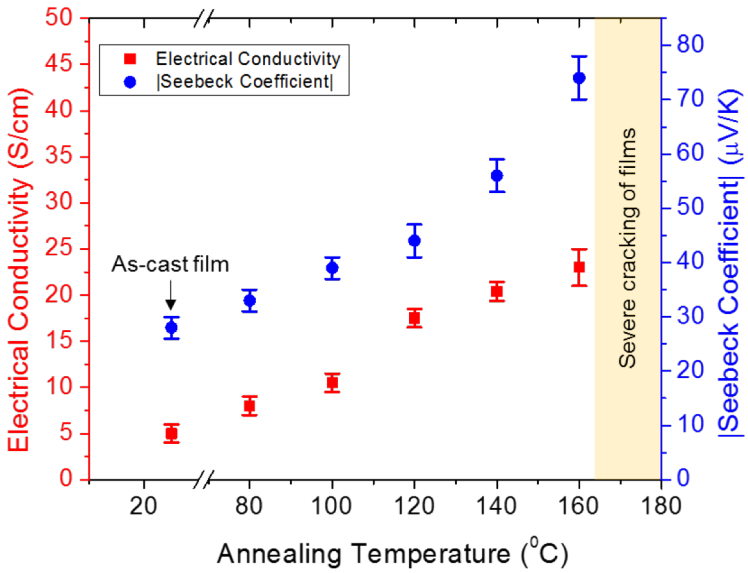


Figure 24. Electrical conductivity and Seebeck coefficient (magnitude) of NiETT/PVDF composite films as a function of annealing temperature. All films are annealed in air for one hour on a hot-plate prior to making thermoelectric measurements.

To isolate changes in NiETT powders from morphological changes in NiETT/PVDF composite films upon annealing, the NiETT powder was first annealed at 160 $^0$C for one hour in air and then cast as a NiETT/PVDF thin film from DMSO that yielded a thermopower of -45 µV/K (Figure 25, sample #3). This is an improvement compared to the control film at -28 µV/K (Figure 25, sample #1) suggesting that a chemical change may be occurring in the NiETT powder when annealed. Upon annealing films prepared with these annealed powders at 160 $^0$C for one hour in air, the thermopower increases to -80 µV/K (Figure 25, sample #4). This reveals

that the underlying mechanism for this enhancement is present in both the NiETT powder itself and in composite form with NiETT/PVDF films.

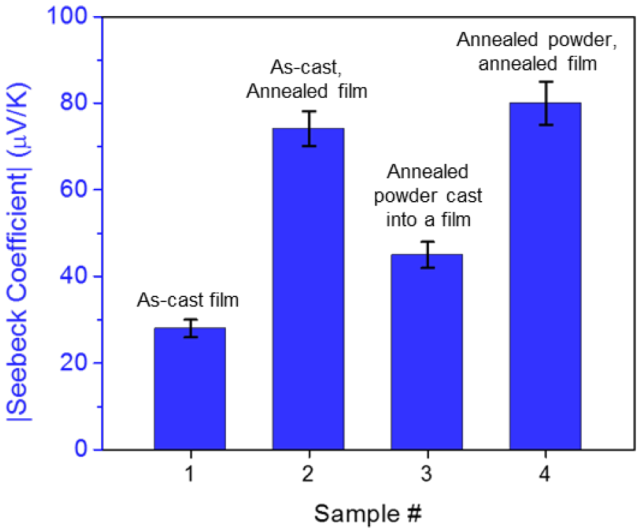


Figure 25. Seebeck coefficient (magnitude) of NiETT/PVDF composite films can be tuned by annealing the pristine powder as well as the film. All samples are annealed in air for one hour on a hot-plate.

*Annealing changes film morphology*

It is known that favourable interaction between the binder and solvent could significantly impact the amount of residual solvent in the film. Given that DMSO is a hygroscopic, low vapor pressure solvent, vacuum drying for 30 minutes may not remove all the solvent. Figure 26 shows SEM images of a NiETT/PVDF film before and after annealing. During the annealing post-treatment process, some of this residual solvent is removed which causes a densification of the film and closes existing cracks (potentially formed from thermal stresses during the original vacuum drying process) present towards the center of the film; some cracks are still observed towards the edges of the film

Annealing just below the melting temperature of PVDF (*i.e.,* at 160 °C) allows NiETT to reorganize into better connected domains. Similar observations have been made with carbon nanotubes in an inert matrix, where the filler reorganizes into more conducting pathways upon annealing.[58, 59] This morphological effect is reflected in a higher $\sigma$ for annealed NiETT/PVDF films compared to as-cast films. However, an increase in the thermopower is also observed, which cannot be explained by reorganized conducting pathways alone; this suggests that another mechanism is present during the annealing process. We hypothesize that annealing results in the removal of volatile impurities in addition to the observed morphological effects, and tandem thermogravimetric analysis – mass spectrometry (TGA-MS) was employed to gain insight into species that are evolved during this annealing process.

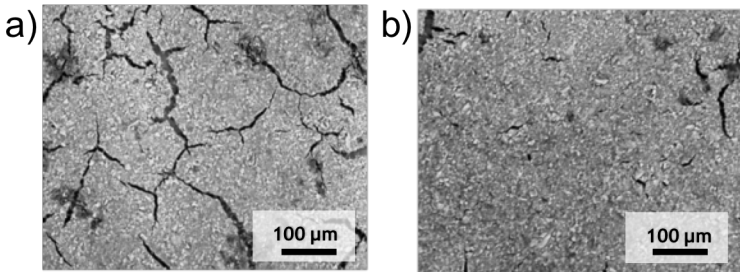


Figure 26. SEM images of NiETT/PVDF composite films a) before annealing and b) after annealing for one hour in air at 160 ° C

*Annealing changes material composition*

Thermogravimetric analysis indicates four mass loss events (Events A-D) occur in the NiETT powder and in the NiETT/PVDF composite films during heating to 600 °C Event A, mimicking the annealing conditions, occurs upon heating to and holding at the annealing temperature of 160 °C for one hour. Event B begins at ~190 °C and shows a peak mass loss rate

at ~235 °C, indicating significant decomposition of the polymer at these temperatures. Event C (peak loss rate at 385 °C) and Event D (peak loss rate at 595 °C in powders, 470 °C in films) are attributed to continued decomposition of NiETT and PVDF. Mass loss Event A is critical to understanding the effect of annealing on NiETT powders and NiETT/PVDF composites.

First, NiETT powder in its original state (Pristine Powder, PP) and NiETT powder after annealing at 160 °C for one hour in air (Annealed Powder, AP) are considered. In these samples, the onset of mass loss is as early as 50 °C (the full duration at half-maximum, FDHM, of the DTG curve is used to identify the temperature range of each event). While this corresponds to the vacuum drying temperature of the films, water is the only signal active at 50 °C.

In pristine powders (PP), Event A is a broad, shallow loss that begins at 70 °C and ends during the isothermal hold, and Figure 27 shows two species are evolved – water and carbonyl sulfide – contributing to a total mass loss of 5.3%. The presence of water is expected as mass losses up to 7% have been previously attributed to water in NiETTs.[43] However, this is the first reported observation of an impurity or decomposition product such as carbonyl sulfide being removed upon annealing a NiETT polymer. The water evolved is hypothesized to be contact moisture; the heating rate (10 K/min) prevents differentiation between water removed at or

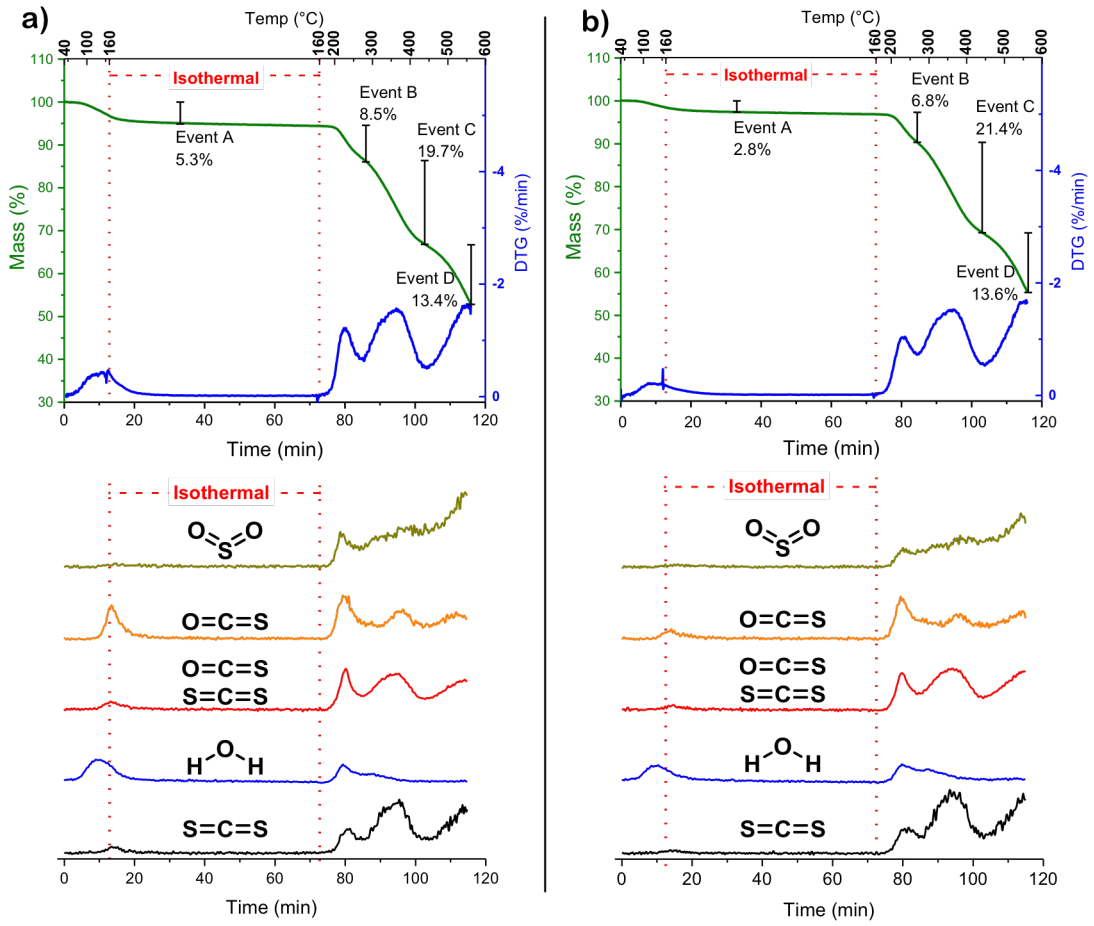


Figure 27. Thermogravimetric analysis with tandem Mass Spectroscopy (TGA-MS) of Pristine Powder (PP) and Annealed Powder (AP) samples of NiETT. (a) TGA with plotted differential (DTG) of PP and normalized ion signals from QMID, (b) TGA with plotted DTG of AP and normalized ion signals from QMID.

below the boiling point (surface or contact moisture) and water removed above the boiling point (incorporated water). For example, $NiSO_4 \cdot 6H_2O$ shows incorporated water removed at 100 – 220 °C and >300 °C;[60] β-$Ni(OH)_2$ shows surface moisture removed at 80 – 90 °C and incorporated water removed at 160 °C; and α-$Ni(OH)_2$ shows incorporated water removed at 240 – 300 °C.[61] The second component, carbonyl sulfide, is an unexpected decomposition product when considering the ideal atomic composition $Na_x[Ni(C_2S_4)]_n$ for these polymers, The source of this signal is potentially from unreacted carbonyl end groups or sulfonyl irregularities[46] in the polymer backbone, as shown in Figure 28. Previous elemental analyses and XPS data support the presence of such impurities.[56] Even in carefully controlled syntheses, impurities and deviations from the idealized structure are present and should be expected.

In anneal powders (AP), Event A consists of 2.8% mass loss during annealing, as shown in Figure 27b, and the signal from carbonyl sulfide is significantly reduced compared to PP. Water, specifically contact moisture, is the major contributor to the 2.8% mass loss, along with small amounts of carbonyl sulfide as evidenced from the MS ion traces for AP. Therefore, the mass loss in PP (5.3%) is approximated to be ~2.8% contact moisture and ~2.5% carbonyl sulfide. This highlights the importance of proper reaction and work-up conditions as well as material post-treatment as removing a small amount of impurity (e.g., carbonyl sulfide) by annealing the NiETT powder increases the thermopower from –28 to –42 μV/K when cast into a film.

Event B (203 – 288 °C FDHM), in both PP and AP, begins the irreversible and destructive decomposition of the NiETT polymer. The onset temperature (180 °C) is recommended as the maximum temperature for any processing method (*e.g.* annealing, printing, extruding) for NiETT. Event B evolves additional water and carbonyl sulfide and begins the release of sulfur dioxide and carbon disulfide. As no combustion is taking place, the water released is expected to originate from incorporated water. The strong signal in Event B from carbonyl sulfide alongside the signals from sulfur dioxide and carbon disulfide indicate that carbonyl sulfide is released as both a beneficial removal of impurities (Event A) and as a destructive decomposition of the NiETT backbone (Event B). The presence of sulfur dioxide provides additional evidence of sulfonyl groups in the backbone, as it is evolved at a lower temperature (200 °C) than sulfur dioxide from $NiSO_4$ decomposition ( >700 °C).[62] The start of evolution of carbon disulfide indicates that the main backbone of NiETT is decomposing at these elevated temperatures. Event C (288 – 444 °C) is a continuation of Event B, and releases additional carbon disulfide, hydrogen sulfide, and sulfur dioxide. The final decomposition, Event D (515 – 600 °C), continues to the end of the run releasing carbon disulfide, sulfur dioxide,

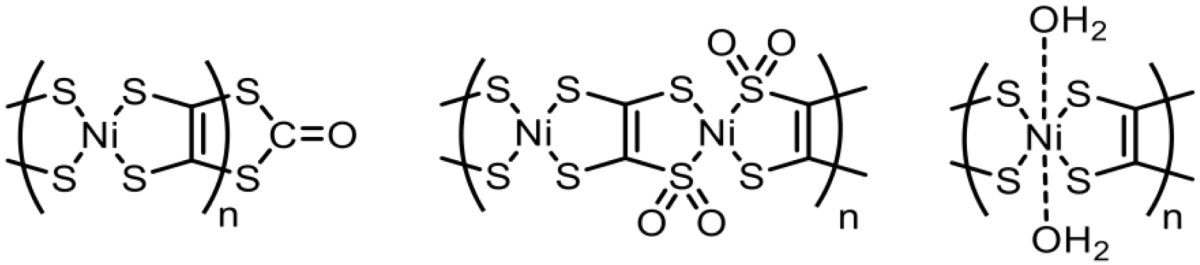


Figure 28. Possible structures present in NiETT that give rise to carbonyl sulfide, water, or sulfur dioxide signals. These are in contrast to the idealized backbone represented by $Na_x[Ni(C_2S_4)]_n$ found in literature.

hydrogen sulfide and water. Based on these observations from TGA-MS, we hypothesize some

additional structures that likely represent these NiETT polymers, shown in Figure 28. Elemental analysis confirms the chemical compositional changes observed in the TGA-MS.

Extending the analysis to composite films, Figure 27 shows the TGA-MS curves with associated ion signals for two film samples: a NiETT/PVDF film cast from DMSO (Pristine Film, PF) and a NiETT/PVDF film cast from DMSO that is annealed at 160 °C in air for one hour (Annealed Film, AF). As in the powder samples, the films show four mass loss events, denoted Events A-D. The signal-to-noise ratio is decreased in these samples due to the small mass of an individual film. We note that the NiETT powder used in both these films is not annealed (similar to PP discussed earlier).

For both film samples, Event A (~80 – 160 °C) aligns with the annealing process, and is crucial for obtaining high thermoelectric properties. Event B (206 – 266 °C) and Event C (346 – 438 °C) are the major NiETT decomposition events that occur after annealing. Both have similar

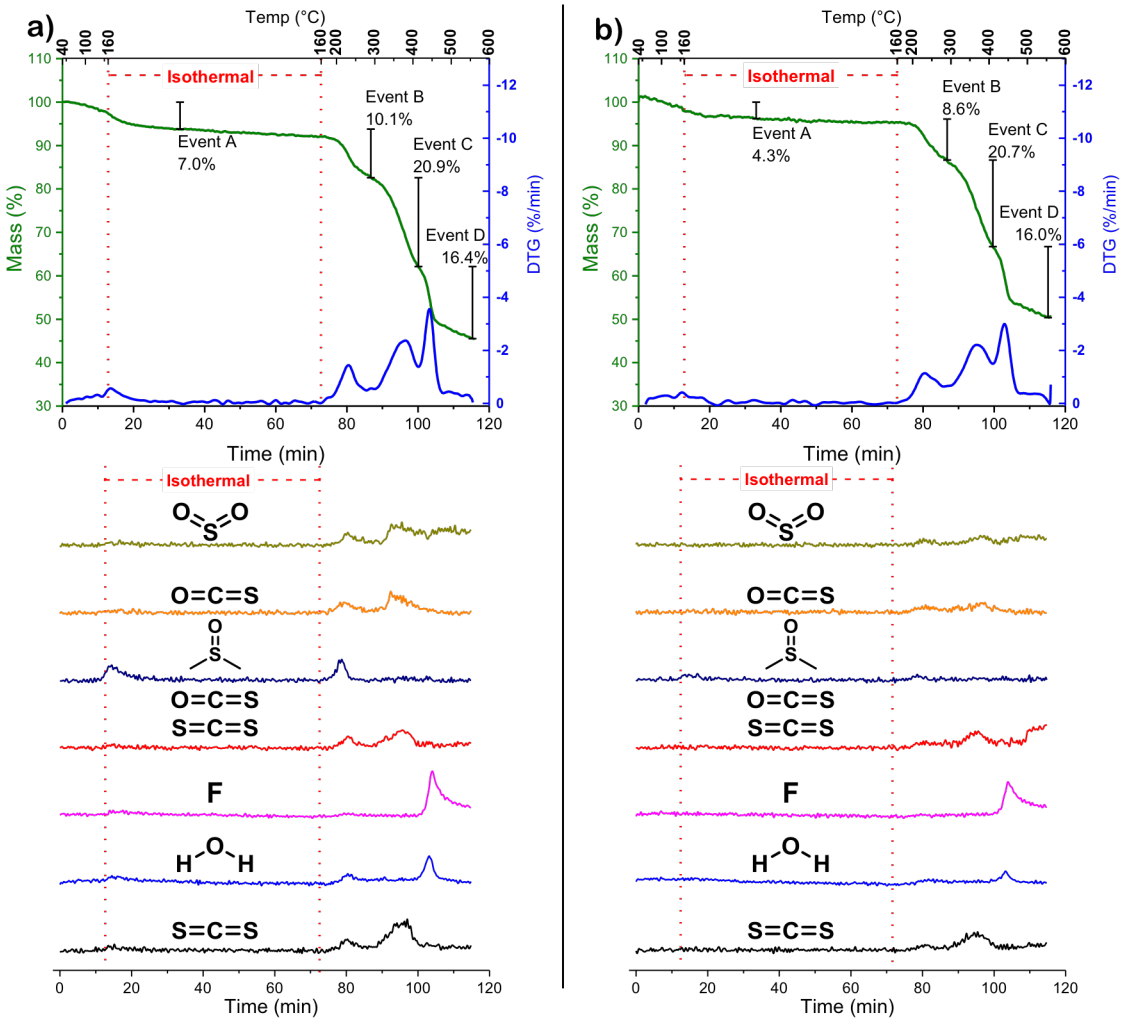


Figure 29. Thermogravimetric analysis with tandem Mass Spectroscopy (TGA-MS) of Pristine Film (PF) and Annealed Film (AF) samples of NiETT/PVDF/DMSO. (a) TGA with plotted differential (DTG) of PF and normalized PF ion signals from QMID, (b) TGA with plotted DTG of AF and normalized AF ion signals from QMID. See Figures S3 and S4 for additional data.

FDHM and peak mass loss temperatures as the powders, confirming that this is a NiETT decomposition. Event D (440 – 487 °C) occurs at a lower temperature in the films that is consistent with the decomposition onset of PVDF.

In pristine films (PF), the mass loss in Event A totals 7.0% and shows a very weak signal of water and almost no signal of carbonyl sulfide when compared to the powder samples. The most prominent mass loss signal during this step is from DMSO. Beyond Event A, during the isothermal hold, there is an additional 1.7% mass loss in PF that is believed to be the slow release of DMSO from the film. In contrast for the annealed films (AF), Event A consists of a smaller mass loss of 4.3%, with no discernable water or carbonyl sulfide signals; the most prominent ion signal is also from DMSO. Less surface moisture is expected to return to the films compared to the powders upon exposure to atmosphere after annealing, as the hydrophobic PVDF surrounding the NiETT particles prevents reabsorption of water. Vacuum drying films at 50 °C for 30 minutes followed by annealing for one hour at 160 °C, does not fully remove DMSO from the composite films. However, complete removal of DMSO is not required to realize the full enhancement in thermoelectric performance. performance

As with the powder samples, Event B in both films (PF and AF) reveals the loss of sulfur dioxide and carbon disulfide from the decomposition of NiETT. The signal for water is minimal in PF and indiscernible in AF; and instead, a signal for DMSO is observed in both. The DMSO released in Event B originates from a separate source more strongly bound within the film (analogous to the incorporated water in PP and AP), as compared to the DMSO released in Event A (which is DMSO trapped within the PVDF). We hypothesize that, in the NiETT powder form, water is bound to both the particle surface and to nickel centers, either in the backbone of the NiETT or as impurities in the film. Annealing the powder removes surface moisture (Event A signals) but does not remove the more strongly bound hydrates (Event B signals). In these powder samples, the surface moisture is rapidly replaced upon cooling in atmosphere causing a similar water signal in both PP and AP in Event A. During the film fabrication process, NiETT experiences a saturated DMSO environment, and contact moisture moves from the surface into the bulk solution. Water bound to nickel centers, both main chain and impurity hydrates, is also exchanged for DMSO. This results in the formation of a nickel-DMSO complex in the film form.[63] complex[63]

When both film samples (PF and AF) are dried at 50 °C under vacuum, the contact moisture and previously bound water is removed along with the majority of DMSO. Some DMSO remains trapped in the PVDF film and is released in PF – Event A, or is bound to nickel centers and released in PF – Event B. For the annealed film, DMSO trapped within the PVDF matrix is readily removed, as evidenced by the rapid decline of DMSO ion signal in AF – Event A, and the significantly smaller DMSO signal in AF – Event B than PF – Event B. This suggests that the process of removing DMSO from the film helps drive the film reorganization, which manifests as a boost in electrical conductivity.

Event C in AF and PF show the same evolution of carbon disulfide and sulfur dioxide as the powder samples, suggesting the NiETT polymer is unaffected by processing into a composite. Event D shows a spike in fluorine signal that matches well with the decomposition of neat PVDF. For the fabrication of thermoelectric devices using NiETT, alternative binders beyond PVDF may be required to address issues such as ink viscosity and solvent compatibility. A preliminary study suggests that the efficacy of annealing is highly dependent of the choice of binder. As such, a systematic study of binder and solvent systems could provide further understanding of this mechanism.

***Charge transport in NiETT/PVDF films***

Temperature dependent $S$ and $\sigma$ measurements were performed to elucidate the charge transport mechanism in annealed NiETT/PVDF composite films. Figure 30 shows the electrical conductivity and Seebeck coefficient magnitude for Na(NiETT) films as a function of temperature.

The electrical conductivity increases with temperature indicating that the transport is thermally activated. In this temperature range, the Seebeck coefficient increases slightly but this increase is within measurement uncertainty limits. This is indicative of semiconducting behavior and follows hopping conduction, as expected for disordered materials. Fitting the temperature dependent data to Mott's variable range hopping model yields a linear fit for a 3D system. However, percolation mechanisms also show a similar power law conductivity dependence, which may be a more accurate description of charge transport in NiETT/PVDF composites due to sample inhomogeneity. Low temperature $S$ and $\sigma$ measurements coupled with gated measurements may be required to fully elucidate the transport mechanism in these materials.

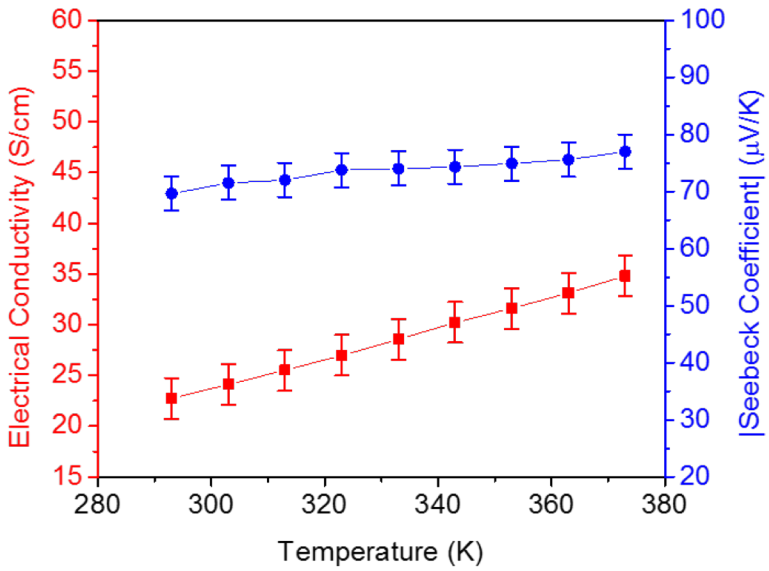


Figure 30. Temperature dependent thermoelectric properties of annealed NiETT/PVDF films are indicative of thermally-activated hopping transport

***References***

1. G. H. Kim, L. Shao, K. Zhang and K. P. Pipe, *Nat Mater*, 2013, **12**, 719-723.
2. M. Neubronner, T. Bodmer, C. Hübner, B. P. Kempa, E. Tsotsas, A. Eschner, G. Kasparek, F. Ochs, H. Müller-Steinhagen, H. Werner and H. M. Spitzner, *Journal*.
3. P. B. Allen, J. L. Feldman, J. Fabian and F. Wooten, *Philosophical Magazine Part B*, 1999, **79**, 1715-1731.
4. I. Stark, M. Stordeur and F. Syrowatka, *Thin Solid Films*, 1993, **226**, 185-190.
5. C. Kittel, *Introduction to solid state physics*, Wiley, Hoboken, NJ, 2005.
6. Z. M. Zhang, *Nano/microscale heat transfer*, McGraw-Hill New York, 2007.
7. R. R. Monchamp, *Journal of Solid State Chemistry*, 1975, **12**, 201-206.
8. J. L. Feldman, M. D. Kluge, P. B. Allen and F. Wooten, *Physical Review B*, 1993, **48**, 12589-12602.
9. J. M. Larkin and A. J. H. McGaughey, *Physical Review B*, 2014, **89**.
10. J. P. Feser and D. G. Cahill, *Review of Scientific Instruments*, 2012, **83**, 104901.
11. D. G. Cahill, S. K. Watson and R. O. Pohl, *Physical Review B*, 1992, **46**, 6131-6140.
12. D. G. Cahill and R. O. Pohl, *Solid State Communications*, 1989, **70**, 927-930.
13. S. P. Inc., HOPG Advanced Ceramics).
14. J. J. Freeman and A. C. Anderson, *Physical Review B*, 1986, **34**, 5684-5690.
15. C. Dames, *Annual Review of Heat Transfer*, 2013, **16**.
16. Y. Ju, K. Kurabayashi and K. Goodson, *Thin Solid Films*, 1999, **339**, 160-164.
17. T. Borca-Tasciuc, A. R. Kumar and G. Chen, *Review of Scientific Instruments*, 2001, **72**, 2139-2147.
18. X. Zhang and C. P. Grigoropoulos, *Review of Scientific Instruments*, 1995, **66**, 1115-1120.
19. K. Kurabayashi, M. Asheghi, M. Touzelbaev and K. E. Goodson, *Journal of Microelectromechanical Systems*, 1999, **8**, 180-191.
20. W. Jang, Z. Chen, W. Bao, C. N. Lau and C. Dames, *Nano Letters*, 2010, **10**, 3909-3913.
21. M. Asheghi, M. N. Touzelbaev, K. E. Goodson, Y. K. Leung and S. S. Wong, *Journal of Heat Transfer*, 1998, **120**, 30-36.
22. X. Zhang, H. Xie, M. Fujii, H. Ago, K. Takahashi, T. Ikuta, H. Abe and T. Shimizu, *Applied Physics Letters*, 2005, **86**, 171912.
23. Y. C. Tai, C. H. Mastrangelo and R. S. Muller, *Journal of Applied Physics*, 1988, **63**, 1442-1447.
24. H. Ushirokita and H. Tada, *Chemistry Letters*, 2016, **45**, 735-737.
25. H. Yan, Z. Chen, Y. Zheng, C. Newman, J. R. Quinn, F. Dotz, M. Kastler and A. Facchetti, *Nature*, 2009, **457**, 679-686.
26. M. C. Stefan, A. E. Javier, I. Osaka and R. D. McCullough, *Macromolecules*, 2009, **42**, 30-32.
27. J. A. Malen, K. Baheti, T. Tong, Y. Zhao, J. A. Hudgings and A. Majumdar, *Journal of Heat Transfer*, 2011, **133**, 081601-081601-081607.
28. S. Kommandur and S. K. Yee, *Journal of Polymer Science Part B: Polymer Physics*, 2017, **55**, 1160-1170.
29. J. E. Mark, *Physical properties of polymers handbook*, Springer, 2007.
30. A. K. Menon and S. K. Yee, *Journal of Applied Physics*, 2016, **119**, 055501.
31. S. LeBlanc, S. K. Yee, M. L. Scullin, C. Dames and K. E. Goodson, *Renewable and Sustainable Energy Reviews*, 2014, **32**, 313-327.

32. S. K. Yee, S. LeBlanc, K. E. Goodson and C. Dames, *Energy & Environmental Science*, 2013, **6**, 2561-2571.
33. J. A. Fan, W.-H. Yeo, Y. Su, Y. Hattori, W. Lee, S.-Y. Jung, Y. Zhang, Z. Liu, H. Cheng and L. Falgout, *Nature communications*, 2014, **5**.
34. K. Yazawa and A. Shakouri, *Environmental Science & Technology*, 2011, **45**, 7548-7553.
35. B. Moon, H. V. Jagadish, C. Faloutsos and J. H. Saltz, *IEEE Transactions on knowledge and data engineering*, 2001, **13**, 124-141.
36. B. Russ, M. J. Robb, F. G. Brunetti, P. L. Miller, E. E. Perry, S. N. Patel, V. Ho, W. B. Chang, J. J. Urban, M. L. Chabinyc, C. J. Hawker and R. A. Segalman, *Advanced Materials*, 2014, **26**, 3473-3477.
37. J. Liu, L. Qiu, G. Portale, M. Koopmans, G. ten Brink, J. C. Hummelen and L. J. A. Koster, *Advanced Materials*, 2017, **29**, 1701641-n/a.
38. D. Yuan, D. Huang, C. Zhang, Y. Zou, C.-a. Di, X. Zhu and D. Zhu, *ACS Applied Materials & Interfaces*, 2017, **9**, 28795-28801.
39. R. A. Schlitz, F. G. Brunetti, A. M. Glaudell, P. L. Miller, M. A. Brady, C. J. Takacs, C. J. Hawker and M. L. Chabinyc, *Advanced Materials*, 2014, **26**, 2825-2830.
40. G. Zuo, Z. Li, E. Wang and M. Kemerink, *Advanced Electronic Materials*, 2018, **4**, 1700501-n/a.
41. A. K. Menon, E. Uzunlar, R. M. W. Wolfe, J. R. Reynolds, S. R. Marder and S. K. Yee, *Journal of Applied Polymer Science*, 2017, **134**.
42. Y. Sun, P. Sheng, C. Di, F. Jiao, W. Xu, D. Qiu and D. Zhu, *Advanced Materials*, 2012, **24**, 932-937.
43. R. Vicente, J. Ribas, P. Cassoux and L. Valade, *Synthetic Metals*, 1986, **13**, 265-280.
44. J. Matienzo, L. I. Yin, S. O. Grim and W. E. Swartz, *Inorganic Chemistry*, 1973, **12**, 2762-2769.
45. H. W. Nesbitt, D. Legrand and G. M. Bancroft, *Physics and Chemistry of Minerals*, 2000, **27**, 357-366.
46. E. J. Uzelac and S. C. Rasmussen, *European Journal of Inorganic Chemistry*, 2017, **2017**, 3878-3883.
47. L. J. Matienzo, W. E. Swartz and S. O. Grim, *Inorganic and Nuclear Chemistry Letters*, 1972, **8**, 1085-1091.
48. W. F. Stickle, J. R. Reynolds and C. A. Jolly, *Langmuir*, 1991, **7**, 2460-2463.
49. S. Sun, P. Wu, D. Zhu, Z. Ma and N. Shi, *Inorganica Chimica Acta*, 1998, **268**, 103-107.
50. P. Sheng, Y. Sun, F. Jiao, C. Di, W. Xu and D. Zhu, *Synthetic Metals*, 2014, **193**, 1-7.
51. G. E. Holdcroft and A. E. Underhill, *Synthetic Metals*, 1985, **10**, 427-434.
52. N. Yoshioka, H. Nishide, K. Inagaki, K. Inagaki and E. Tsuchida, *Polymer Bulletin*, 1990, **23**, 631-636.
53. P. Sheng, Y. Sun, F. Jiao, C. Liu, W. Xu and D. Zhu, *Synthetic Metals*, 2014, **188**, 111-115.
54. N. Toshima, K. Oshima, H. Anno, T. Nishinaka, S. Ichikawa, A. Iwata and Y. Shiraishi, *Advanced Materials*, 2015, **27**, 2246-2251.
55. K. Oshima, Y. Shiraishi and N. Toshima, *Chemistry Letters*, 2015, **44**, 1185-1187.
56. A. K. Menon, R. M. W. Wolfe, S. R. Marder, J. R. Reynolds and S. K. Yee, *submitted to Advanced Functional Materials*, 2018.
57. F. Jiao, C. A. Di, Y. Sun, P. Sheng, W. Xu and D. Zhu, *Philosophical transactions. Series A, Mathematical, physical, and engineering sciences*, 2014, **372**, 20130008.

58. Y. Pan, H. K. F. Cheng, L. Li, S. H. Chan, J. Zhao and Y. K. Juay, *Journal of Polymer Science Part B: Polymer Physics*, 2010, **48**, 2238-2247.
59. F. Jiang, L. Zhang, Y. Jiang, Y. Lu and W. Wang, *Journal of Applied Polymer Science*, 2012, **126**, 845-852.
60. P. N. Nandi, D. A. Deshpande and V. G. Kher, *Thermochimica Acta*, 1979, **32**, 143-149.
61. D. S. Hall, D. J. Lockwood, C. Bock and B. R. MacDougall, *Proceedings of the Royal Society A: Mathematical, Physical and Engineering Science*, 2015, **471**.
62. E. Tomaszewicz and M. Kotfica, *Journal of Thermal Analysis and Calorimetry*, 2004, **77**, 25-31.
63. D. W. Meek, D. K. Straub and R. S. Drago, *Journal of the American Chemical Society*, 1960, **82**, 6013-6016.